

**UNIVERSIDAD AUTÓNOMA DE BAJA CALIFORNIA**  
PROGRAMA DE MAESTRÍA Y DOCTORADO EN CIENCIAS E INGENIERÍA  
FACULTAD DE INGENIERÍA



**TESIS:**

**AERODYNAMIC OPTIMIZATION OF RAM AIR TURBINE  
ROTOR OF A COMMERCIAL AIRCRAFT**

Que presenta para obtener el grado de MAESTRO EN CIENCIAS

**TESISTA**

Mariana Glenda Avila Zayas

**DIRECTOR DE TESIS**

Dra. Miriam Siqueiros Hernández

**CODIRECTOR DE TESIS**

Dr. Emmanuel Santiago Durazo Romero

Mexicali, Baja California, diciembre 2023



**AERODYNAMIC OPTIMIZATION OF RAM AIR TURBINE  
ROTOR OF A COMMERCIAL AIRCRAFT**

**Mariana Glenda Avila Zayas**

A Thesis submitted for the degree of Master by Research (ResM)

in the

School of Engineering and Material Science

Queen Mary University of London

and

*Universidad Autónoma de Baja California*

QMUL supervisor: Dr. Eldad Avital

UABC supervisor: Dr. Miriam Siqueiros Hernández

December 2023



Universidad  
Autónoma de  
Baja California



Queen Mary  
University of London

**AGREEMENT OF COOPERATION FOR THE ESTABLISHMENT OF  
POSTGRADUATE PROGRAMME BETWEEN**

**UNIVERSIDAD AUTÓNOMA DE BAJA CALIFORNIA,  
ACTING THROUGH ITS RECTOR DR. DANIEL OCTAVIO VALDEZ DELGADILLO  
Edificio de Rectoría, Avenida Álvaro Obregón, sin número,  
Colonia Nueva, C.P. 21100, Mexicali, Baja California, México**

And

**QUEEN MARY UNIVERSITY OF LONDON, ACTING THROUGH THE FACULTY OF SCIENCE  
AND ENGINEERING of Mile End Road, London E1 4NS (referred to as Queen Mary)**

*Universidad Autónoma de Baja California (UABC) acting through its Rector Dr. Daniel Octavio Valdez Delgadillo and University of Queen Mary of London acting through the Faculty of Science and Engineering (QMUL) of The United Kingdom of Great Britain and Northern Ireland, hereinafter referred to as 'the Parties'.*

**RECOGNIZING** that granting fellowships to Mexican citizens to facilitate postgraduate studies in The United Kingdom of Great Britain and Northern Ireland will contribute to the enhancement of the relationship between both Nations;

**TAKING INTO CONSIDERATION** the provisions of the Basic Agreement of Scientific and Technological Cooperation between the Government of the United Mexican States and the Government of the United Kingdom of Great Britain and Northern Ireland, signed in Mexico City on the 25th of February, 1975;



**ARTICLE 15**  
**FINAL PROVISIONS**

This Agreement will enter into force on the date of its signing and is valid for 5 years from the date that is it signed. It may be extended by written agreement, before its expiration, by mutual consent and after an evaluation of the results of the Agreement.

This Agreement may be modified by mutual consent of the Parties, formalized through written communications specifying the date on the entry into force of such modifications.

If either Party decides to terminate this Agreement, it must be done so by written communication addressed to the other Parties six (6) months in advance. Early termination of this Agreement will not affect the conclusion of the activities formalized while it was in force.

Signed on the 17<sup>th</sup> of March of 2021 in, all texts being equally authentic.

**UNIVERSIDAD AUTÓNOMA DE BAJA  
CALIFORNIA**

daniel valdez (Mar 17, 2021 10:29 PDT)

**Dr. Daniel Octavio Valdez Delgadillo**  
**Rector**

**QUEEN MARY UNIVERSITY OF LONDON**

**Professor Colin Bailey**  
**President and Principal**

**UNIVERSIDAD AUTÓNOMA DE BAJA  
CALIFORNIA**

**Dr. David Guadalupe Toledo Sarracino**  
**Academic Cooperation and Education Liaison**  
**Director**  
**Witness**

**Dr. Juan Guillermo Vaca Rodriguez**  
**Office of Research and Postgraduate Director**  
**Witness**

## **Declaration**

I, Mariana Glenda Avila Zayas, confirm that the research included within this thesis is my own work or that where it has been carried out in collaboration with, or supported by others, that this is duly acknowledged below and my contribution indicated.

I attest that I have exercised reasonable care to ensure that the work is original and does not to the best of my knowledge break any UK law, infringe any third party's copyright or other Intellectual Property Right, or contain any confidential material.

I accept that Queen Mary University of London and Universidad Autónoma de Baja California, have the right to use plagiarism detection software to check the electronic version of the thesis.

I confirm that this thesis has not been previously submitted for the award of a degree by this or any other university.

The copyright of this thesis rests with the author and no quotation from it or information derived from it may be published without the prior written consent of the author.

Mariana Glenda Avila Zayas

October, 2023

## Abstract

Ram Air Turbines (RATs) are employed to supply power for auxiliary and backup systems of an aircraft in case of a major power shortage. These turbines are commonly Horizontal Axis Wind Turbines (HAWTs). In this study, we investigate the performance of a RAT under cruise altitude operating conditions. CFD-RANS computations coupled with Blade Element Method (BEM) are conducted to examine the impact of adding Gurney flaps (GF) to the rotor blades in terms of power and drag (thrust) performance. Three different GF height configurations of 1% chord (1%c), 3%c, and 5%c are applied to the blades of a small RAT. The rotor diameter is 1.016 meters, comprising of two blades with a constant chord length of 0.127 meters and a NACA 8318 airfoil, featuring twist angle along the blade span. The effects of the Gurney flaps are explored over a Reynolds number range of 200k to 500k based on the chord length, corresponding to the Reynolds number of the relative wind speed around the blade at sections of 25%, 50%, 75% and 100% of the blade. Lift coefficient ( $C_L$ ) and drag coefficient ( $C_D$ ) results were imported to Qblade to perform a BEM turbine analysis. The results demonstrate a noticeable increase in the maximum coefficient of power around tip speed ratio (TSR) of 3. Also, a comparison was made between a clean blade and a blade with GF mounted only at the root of the blade. The blade with GF representing 1% of the chord, mounted at the root of the blade yields improved  $C_P/C_T$  for a wider range of  $3 < \text{TSR} < 6.6$ . However, a GF with height of 5%c exhibits the highest  $C_P/C_T$  ratio, both at low TSR (ranging from 1 to 1.8) and high TSR (from 4 to 7.6). Data validation was conducted for the NACA 8318 airfoil using experimental results from Yoshida (2000). Additionally, data validation was also performed by comparing the findings with CFD data from Shen (2016) for E387 airfoil performed on the low-speed wind tunnel of Queen Mary University of London. These validations aim to support and validate the results obtained within this thesis.

## **Acknowledgements**

I would like to express my deepest gratitude to both of my supervisors. To Dr. Miriam Siqueiros for guiding me during the first year of my master's and for sharing her knowledge with me, always looking for ways to help me in my professional path. To Dr. Eldad Avital for his infinite patience and mentorship, for guiding me and showing me the right direction within my research and always showing support to my research needs. Also I want to express my gratitude to Dr. Emmanuel Durazo, for introducing me to the dual master program and kindly providing me his help during the process.

Special thanks to Dr. Alejandro Ortiz for teaching me the bases of fluid dynamics and BEM theory during my first year of research.

Also, I'll like to thank all my colleagues and professors that have helped me along the way, sharing with me their knowledge.

Finally, I want to express my infinite gratitude to my parents, who always provide me with support and love. To both of my brothers for always being there for me when I needed it and to my husband, for his patience and support along the way.

This project was funded by:

Universidad Autónoma de Baja California and Queen Mary University of London Dual Master scholarship program;

Consejo Nacional de Ciencia y Tecnología (CONACYT) scholarship;

And Global Sustainable Electricity Partnership (GSEP) grant.

## **Dedications**

To my parents, Glenda and Felipe, and to my dear Husband, Guillermo.

# Contents

<b>1.</b>	<b>Introduction.....</b>	<b>1</b>
1.1	History of RATs usage.....	3
1.2	Motivation.....	5
1.3	Objectives.....	5
1.3.1	Specific objectives.....	6
1.4	Thesis outline .....	6
<b>2.</b>	<b>Literature review .....</b>	<b>7</b>
2.1	Wind turbines.....	10
2.2	RAT design and analysis.....	12
2.3	Operating conditions study .....	16
2.4	Gurney flaps.....	18
<b>3.</b>	<b>Computational methodology.....</b>	<b>20</b>
3.1	Introduction.....	20
3.2	Governing equations .....	21
3.3	Turbulence models.....	22
3.3.1	Model $k - \omega$ .....	23
3.3.2	Model SST $k - \omega$ .....	24
3.4	Blade Element Momentum .....	24
3.5	Computational Fluid Dynamics.....	26
3.6	Ram power .....	27
3.7	Power coefficient.....	27
3.8	Aerodynamic coefficients.....	28
3.8.1	Lift coefficient .....	28
3.8.2	Drag coefficient .....	29
3.9	Turbine blades.....	29
3.10	Summary .....	31

<b>4.</b>	<b>Analysis and experimentation for problem solving.....</b>	<b>32</b>
4.1	Introduction.....	32
4.2	NACA 8318 Computational.....	33
4.2.1	Initial turbine specifications.....	33
4.2.2	Isolated airfoil.....	34
4.2.3	Operating conditions.....	36
4.2.4	Computational 2D domain.....	37
4.2.5	Mesh generation.....	37
4.2.6	Boundary conditions.....	40
4.2.7	Results.....	41
4.2.8	Data validation of NACA 8318.....	50
4.3	E387 Computational.....	51
4.3.1	Geometry.....	52
4.3.2	Domain.....	52
4.3.3	Mesh.....	52
4.3.4	Boundary conditions.....	54
4.3.5	Data validation of E387.....	54
4.4	Turbine performance analysis with BEM Method.....	56
4.4.1	Turbine design in Qblade.....	56
4.4.2	Turbine performance.....	57
4.5	Summary.....	62
<b>5.</b>	<b>Conclusions and Future work.....</b>	<b>64</b>
5.1.	Discussion and conclusions.....	64
5.2.	Future work recommendations.....	65
<b>6.</b>	<b>List of references.....</b>	<b>67</b>

## List of Figures

Figure 1.1. RAT for military application on a USAF F-105 (Bolognesi et al., 2009).....	4
Figure 1.2. RAT in commercial application on BOEING 757 (Bolognesi et al., 2009) .....	5
Figure 2.1. Transversal section of a Ram Air Turbine assembly and their components (Harrington & bai, 2019) .....	7
Figure 2.2. Cross section of a blade that illustrates velocities (relative wind speed $W$ , wind speed $V$ , axial wind speed $v$ , and tangential wind speed $u$ ) and angles (Pitch angle $\theta$ , Angle of attack $\alpha$ , and relative wind angle $\phi$ ) at a specific distance ( $r$ ) from the axis of the rotor (Gundtoft, 2009). .....	8
Figure 2.3. Thrust force decomposed along the rotor axis (Gundtoft, 2009). .....	9
Figure 2.4. Three-blade horizontal Axis Wind Turbine (M. F. Ismail, 2014). .....	11
Figure 2.5. Three-blade vertical Axis Wind Turbine (M. F. Ismail, 2014). .....	11
Figure 3.1. Typical shape of a turbine blade and the classification of its regions (Schubel & Crossley, 2012). .....	30
Figure 4.1. Pitch angle variation along the blade span in m. ....	34
Figure 4.2. Airfoil with GF dimensions expressed in mm, at height configurations of (a) 1% $c$ , (b) 3% $c$ and (c) 5% $c$ . .....	35
Figure 4.3. Dimensions of the C-type 2D computational domain based on the chord length ( $c$ ) of the airfoil. The dimensions are indicated from the point where the trailing edge of the airfoil is expected to be, extending outward to the exterior.....	37
Figure 4.4. Overview of structured mesh for NACA 8318 airfoil.....	39
Figure 4.5. Detail of structured mesh for NACA 8318 with GF at 1% $c$ airfoil. ....	39
Figure 4.6. NACA 8318 $C_L$ vs AoA variation with GF configuration at $Re=217,530$ . .....	42
Figure 4.7. NACA 8318 $C_D$ variation with AoA for airfoil configurations at $Re=217,530$ . .....	42
Figure 4.8. NACA 8318 $C_L$ to $C_D$ ratio variation with AoA for airfoil configurations at $Re=217,530$ . .....	43
Figure 4.9. $C_L$ variation with the Reynolds number for NACA 8318 clean airfoil. ....	44
Figure 4.10. $C_L$ variation with the Reynolds number for NACA 8318 with GF at 1% $c$ . ....	45
Figure 4.11. $C_D$ variation with the Reynolds number for NACA 8318 with GF at 1% $c$ . ....	45
Figure 4.12. $C_L$ variation with the Reynolds number for NACA 8318 with GF at 5% $c$ . ....	46
Figure 4.13. $C_D$ variation with the Reynolds number for NACA 8318 with GF at 5% $c$ . ....	46
Figure 4.14. Pressure coefficient distribution on the airfoil at AoA=9 at 217,530 $Re$ along the chord (m).....	47
Figure 4.15. Flow around the T.E. at AoA=9 degrees for (a) Clean airfoil, (b) GF 1% $c$ , (c) GF 3% $c$ , (d) GF 5% $c$ . .....	48
Figure 4.16. Vortex formation visualization in the T.E. of (a) Clean airfoil and (b) airfoil with GF at 5% $c$ length. ....	49
Figure 4.17. Comparison of $C_l$ vs AoA for NACA 8318 at 500k $Re$ at $M=0.058$ . .....	51
Figure 4.18. Overview of structured mesh for E387 airfoil.....	53
Figure 4.19. Detail of structured mesh for E387 airfoil.....	53

Figure 4.20. $C_L$ vs AoA for E387 at $Re=100$ k.....	55
Figure 4.21. $C_D$ vs AoA for E387 at 100k.....	55
Figure 4.22. Power Coefficient variation with TSR for airfoil without and with GF at heights of 1%, 3% and 5%c.....	59
Figure 4.23. Thrust Coefficient variation with TSR for Turbine blades without and with GF at heights of 1%, 3% and 5%c.....	59
Figure 4.24. Pressure Coefficient to Thrust Coefficient ratio vs TSR for turbine blades without and with GF at heights of 1%, 3% and 5%c.....	60
Figure 4.25. $C_P/C_T$ ratio comparison for GF height of 1%c mounted at either the root or the tip of the blade and original blade.....	61
Figure 4.26. $C_P/C_T$ ratio comparison for original blade and different blade configurations with GF with heights of 1%, 3% and 5%c mounted at the root of the blade.....	61

## List of tables

Table 4.1. Gurney flap dimensions.....	35
Table 4.2. Turbine operating conditions.....	36
Table 4.3. Air properties at 10,000 m (Cengel, 2006). .....	36
Table 4.4. Height of first grid cell variation at different sections of the blade.....	38
Table 4.5. Velocity of the flow around the blade at blades section of 25, 50, 75 and 100%. .....	40
Table 4.6. Mesh sensitivity study results for NACA 8318 airfoil at 500k Re at AoA=0 Deg. .....	50
Table 4.7. Mesh sensitivity study results for E387 airfoil at an angle of attack of 0°. .....	52
Table 4.8. Data comparison of E873 CFD simulation and experimental test at an angle of attack of 0°. .....	54
Table 4.9 Blade design specifications.....	57
Table 4.10. Comparison of maximum $C_P$ , $C_T$ and $C_P/C_T$ ratio for four blade configurations at different TSR. ....	58
Table 4.11. Minimum (Saad et al., 2017) and maximum operating condition for RAT. ....	63

## Nomenclature

AoA	Angle of Attack
BEM	Blade Element Momentum
CAD	Computer Aided Design
CFD	Computational Fluid Dynamics
GF	Gurney Flap
HAWT	Horizontal Axis Wind Turbines
L.E.	Leading Edge
M	Mach Number
RANS	Reynolds Average Navier Stokes equations
RAT	Ram Air Turbine
Re	Reynolds Number
RPM	Revolutions per minute
SST	Shear Stress Transport
T.E.	Trailing Edge
TSR	Tip speed ratio
VAWT	Vertical Axis Wind Turbine

## Symbols

$a$	Axial interference factor
$a'$	Tangential interference factor
$c$	Airfoil chord
$C_D$	Drag Coefficient
$C_L$	Lift Coefficient
$C_P$	Power Coefficient
$C_D'$	Drag coefficient for a 2D body (chapter 3)
$C_L'$	Lift coefficient for a 2D body (chapter 3)
$C_T$	Torque coefficient
$\underline{P}$	Actual power extracted from the wind
$P_{th}$	Maximum theoretical power extracted from the wind
$\bar{p}$	Mean pressure
$q_\alpha$	Dynamic pressure
$R$	turbine radius
$R_{ij}$	Reynolds stress
$S_{ij}$	Strain tensor
$u$	Tangential wind speed (chapter 2)
$v$	Axial wind speed
$V$	Wind speed
$W$	Relative wind speed
$y^+$	Dimensionless wall distance
$S$	Reference area of the rotor
$T$	Thrust
$\bar{u}_i$	Mean velocity

## Greek symbols

$\nu_T$	Turbulent eddy viscosity
$\tau_{ij}$	Stress tensors
$\mu$	Dynamic viscosity
$\theta$	Pitch angle
$\Phi$	Wind angle
$\kappa$	Kinetic energy
$\nu$	kinematic viscosity
$\omega$	Dissipation rate
$\omega$	angular speed of the rotor

# Chapter 1

## 1. Introduction

The Ram Air Turbine (RAT) is a small rotor that falls within the category of Horizontal Axis Wind Turbine (HAWT). This rotor is stored in a compartment on the fuselage or wing of a commercial aircraft under normal flight conditions. However, in the event of significant engine power failure, the RAT is deployed to primarily provide emergency power to essential electrical systems to ensure a safe landing, hence as the tendency of more electrical aircraft increase, the importance of RAT in emergency situations rises.

There is a constant need in aviation to reduce the climate impact and carbon emissions. In the sustainable aviation (SA) report (2020), established that UK aviation is aiming to achieve net zero emissions by 2050. This goal involves working towards carbon removal initiatives. The UK aviation have the initiative to reduce by 2050, 26.4 million Tons of carbon dioxide (MtCO<sub>2</sub>) by implementing sustainable aviation fuels and 10.6 MtCO<sub>2</sub> by introducing more efficient electrical aircrafts. Therefore, aircraft are increasingly relying on electric power to manage their flight control systems, usually used during landing, elevating the importance of availability of electrical power in cases of forced landings due to engine failure.

The Ram Air Turbine (RAT) is one of the potential mechanisms that are applicable to generate renewable energy on an aircraft, as it extracts power from the air stream. However, there is a constant need to improve the efficiency and power output of RATs enabling them to extract more power from the air, specially at low speeds where it can only generate around 400 W (Saad et al., 2017).

In the pursuit of improving the performance and efficiency of RATs, aerodynamic enhancements play a crucial role in increasing the power generation of the turbine. In this study, an aerodynamic enhancement device called Gurney Flap (GF) will be implemented to study the effect on the efficiency of the RAT.

Gurney Flaps, introduced by Dan Gurney in the 1960s to improve the performance of racing cars, are small tabs typically added to the trailing edge of an airfoil. The height of the GF is a percentage of the airfoil chord ( $c$ ), which is described as a straight line that goes from the front edge of the airfoil (leading edge) to the back edge (trailing edge). For wind turbines, the GF height varies between 1 to 5 percent of the chord length ( $\%c$ ). In this study, the GF will be added to a NACA 8318 airfoil.

An airfoil is the transverse shape of a blade or a wing. This shape is designed to generate lift, creating a pressure difference between the upper and lower surface of the airfoil when the air flows around it. Airfoils come in a variety of shapes depending on their purpose. The National Advisory Committee for Aeronautics (NACA) has a series of characterized airfoils classified in different families. The NACA 8318 airfoil belongs to the NACA 4-digit family and refers to a specific airfoil shape where 8318 indicates geometric features of the airfoil.

The power coefficient ( $C_p$ ) of the RAT is a parameter that determines the efficiency of the turbine, it describes the relation of the actual power extracted from the air and the maximum theoretical power. When designing the turbine, one of the primary goals is to increase this parameter. However, there is a limit to the amount of power that a turbine can extract from the airstream, if the turbine were to capture a 100% of the power from the airstream, the consequence would entail a cessation of the airstream, thereby, the blades would slow down, making this 100% turbine's efficiency unfeasible. BETZ theory explains the existence of a theoretical maximum power that a turbine can capture from the air, which is approximately  $16/27$  of the energy present in the air (X. Zhang et al., 2018). This maximum power is commonly referred to as the BETZ limit.

The calculation of the efficiency of a turbine can be done with different methods. Blade Element Momentum (BEM) method is the one that is going to be used in this work to calculate the power output of the turbine. This method consists of dividing the turbine blade into smaller sections, referred to as elements, to analyze the forces acting upon each individual section. By calculating the forces, such as lift and drag, acting on these elements, the method then consolidates these calculated forces across all sections to determine the combined force generated by the entire blade. Ultimately, this approach allows for the

estimation of the total power generated by the turbine based on the collective forces exerted by its individual blade elements. This method requires low computational power, provides reasonably accurate results and is much less time-consuming than Computational Fluid Dynamics (CFD). However, BEM method doesn't account for complex unsteady phenomena, which can interfere in the accuracy of the results in more complex cases.

CFD is a numerical method that employs Navier-stokes equations to predict the behavior of a fluid around an object under specified physical conditions. Performing numerical methods is more cost-effective than performing experimental tests, it is a valuable alternative to conserve resources while providing insights of the aerodynamics of a given geometry. This study adopts a two-step approach: firstly, utilizing CFD to derive the aerodynamic forces acting on individual airfoils. Subsequently, the obtained aerodynamic force coefficients are transferred to QBlade, a software employing the BEM method. This sequential process facilitates the computation of overall turbine efficiency while obtaining the benefits on the accuracy of the CFD for individual airfoil elements, it also leverages the time efficiency advantage of the BEM method.

## **1.1 History of RATs usage**

RATs were first employed as an additional power source exclusively for military aircraft (Fig. 1.1) in 1943 (Saad et al., 2017). The ME 163B Komet became the first aircraft to have a RAT installed. It was during the 1960s that RATs began to be utilized as emergency power generators, and it wasn't until the 1980s that RATs started being used in commercial aircraft (Saad et al., 2017). The Boeing 757 and 767 are examples of commercial aircraft that employ RATs, which are deployed at a minimum speed of 80 knots (41.16 m/s). This speed represents the minimum operational requirement for RATs in Boeing 757 (see Figure 1.2) and 767 models (Saad et al., 2017).



**Figure 1.1.** RAT for military application on a USAF F-105 (Bolognesi et al., 2009).

Over the past few decades, there have been multiple instances showcasing the utilization of RATs (Ram Air Turbines) in emergency situations. For instance, in 1983, an Air Canada Boeing 767 effectively deployed its RAT at an altitude of 41,000 ft (12,500 m) (Saad et al., 2017). Similarly, in 2001, an Airbus A330 encountered a failure at 39,000 ft (11,887 m), but the RAT helped to achieve a successful landing (Saad et al., 2017). Another notable incident took place in 2016 when Air Canada utilized the RAT on their Embraer ERJ-190-100 aircraft at an altitude of 36,000 ft (10,972 m) (Transportation Safety Board of Canada., 2017). These examples highlight the importance of RATs in emergency scenarios.



**Figure 1.2.** RAT in commercial application on BOEING 757 (Bolognesi et al., 2009)

## **1.2 Motivation**

Currently, most commercial aircraft have RATs installed as backup power generators, these are deployed during mayor power loss on flights as an emergency power generation mechanism to ensure the aircraft land safely. Although small HAWTs are a reliable mechanism to extract energy from the airstream, the amount of energy that can be obtained is constrained by BETZ limit that states that a wind turbine can capture a maximum of  $16/27$  of the energy available in the air and convert it into electrical energy (White, 2011), in addition to this, RATs reduce their efficiency at low speeds, achieving an output power around 400W at low-speed applications. It is sought a better turbine efficiency under low-speed operational conditions given that in case of engine failure when RAT is deployed, the aircraft will experience a decrease in the flight speed.

## **1.3 Objectives**

The aim of this project is to enhance the aerodynamic performance of the RAT while the aircraft operates at low cruise speeds (60 m/s), corresponding to a Reynolds of 217,564, expecting to see an increase in the  $C_P/C_T$  ratio while maintaining a high  $C_P$ . This will be achieved by following the specific objectives shown in section 1.3.1.

### **1.3.1 Specific objectives**

- 1 Conduct two dimensional computations of the airfoil NACA 8318, with clean airfoil and with Gurney flaps at three heights 1, 3 and 5% $c$ .
- 2 Pursue full turbine calculations using BEM method in Qblade software, using  $C_L$  and  $C_D$  data obtained from 2D computations at each section of the turbines blade.
- 3 Determine the effect of Gurney Flap in the output Power Coefficient ( $C_P$ ) and the  $C_P/C_T$  ratio of the RAT.

### **1.4 Thesis outline**

This study consists of the study of the aerodynamic effects of Gurney Flaps (GF) implemented on small commercial Ram Air Turbine (RAT) in the output Power Coefficient ( $C_P$ ). This thesis is divided into five chapters.

The first chapter consists of the introduction to the RAT concept and its importance in aviation industry. Within this chapter the motivation and objectives of this work are mentioned. The second chapter contains a review of relevant work made in the past regarding RAT and HAWT enhancement, the operational conditions at which these rotors were study and the computational fluid dynamics (CFD) techniques implemented in the study of RATs. Chapter three details the theory of the computational methods used in this study to analyze the RAT, these methods being the Reynolds-Averaged Navier stokes (RANS) solvers and the blade element momentum (BEM) method. Chapter four contains an insight into the aerodynamics of the NACA 8318 airfoil, with and without GF at heights of 1%, 3% and 5% $c$ , by performing two-dimensional CFD, as well as the analysis of the whole turbine using Blade Element Momentum (BEM) method, where a comparison of the coefficient of power ( $C_P$ ) to coefficient of thrust ( $C_T$ ) ratios for the four blade configurations (clean and with GF at three different heights) were made. Finally in chapter five, a discussion of the results and future work recommendations are provided.

## Chapter 2

### 2. Literature review

Ram Air Turbines (RAT) are classified as small Horizontal Axis Wind Turbines (HAWT), mounted on the aircraft to extract energy from the airstream, and convert the mechanical energy generated by the rotation of the rotor into electrical energy (Saad et al., 2017). These turbines consist of two or three blades. The blades are attached to a hub located at contact of the turbine, and it's connected to the main axis of the drivetrain (Jiménez-Ramírez et al., 2016) (Fig. 2.1). The drivetrain links mechanically the rotor to the generator or pump, with the objective of transmitting the Thrust to the generator (Harrington & Baines, 2019) .

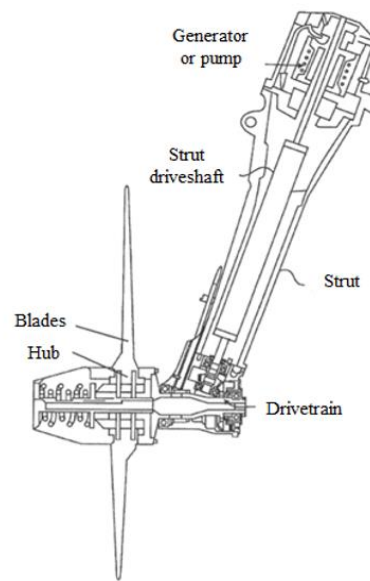


**Figure 2.1.** Transversal section of a Ram Air Turbine assembly and their components (Harrington & bai, 2019)

The RAT (Figure 2.1) is automatically deployed in emergency situations when the aircraft experiences total or mayor loss of power, engine failure, loss of hydraulic pressure or gas shortage in the combustion chamber (Parés Prat, 2012). These turbines are mainly employed to supply power to auxiliary and backup systems of an aircraft, like surface controllers, avionics, pneumatic pumps, navigation, and communication equipment (Valencia et al., 2020). It is common in commercial aircraft to use the RAT as a main

emergency power supply method, due features as; unlimited power duration, low manufacturing costs and the advantage that this turbine does not require fuel to function (Altoma & Alhakeem, 2019).

A RAT's good performance depends on the lift force that is generated in the blades. In the design phase of these turbines, the objective is to minimize the turbulence caused by the separation of the flow from the blade, therefore different methods are sought to enhance the performance through blade shape and angle modifications (Jiménez-Ramírez et al., 2016). The methods of studying the performance of the RAT blades, mainly consist of performing theoretical, numerical, and experimental studies (X. Zhang et al., 2018).

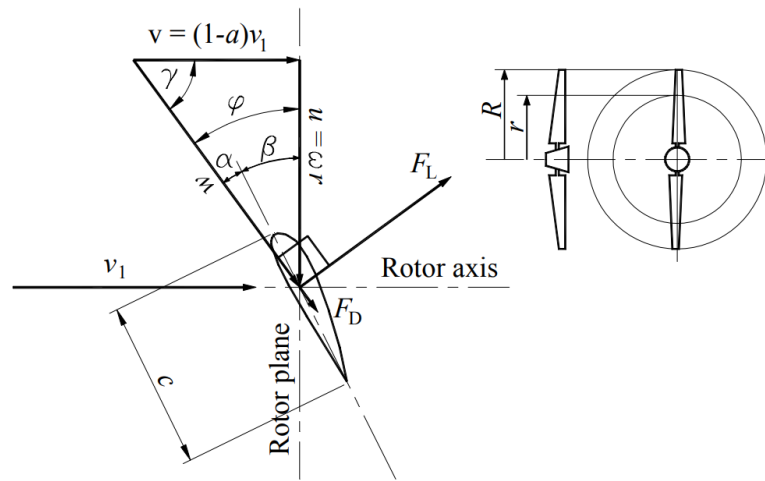


**Figure 2.2.** Cross section of a blade that illustrates velocities (relative wind speed  $W$ , wind speed  $V$ , axial wind speed  $v$ , and tangential wind speed  $u$ ) and angles (Pitch angle  $\theta$ , Angle of attack  $\alpha$ , and relative wind angle  $\phi$ ) at a specific distance ( $r$ ) from the axis of the rotor (Gundtoft, 2009).

The  $C_p$  is one of the most important parameters that indicates the efficiency of the turbine. Is one of the main parameters investigated in this study. Further details on  $C_p$  are shown in section 3.7.

Usually, the output power that a RAT can generate can vary in the range of 5-100 kw, this amount, it's the sufficient to allow a safe landing in the case of an emergency (Renganathan et al., 2014). However, it has been found that when the aircraft is operating at

low speeds, the amount of output power that the RAT generates is around 400 W (Saad et al., 2017). Because of this, research of RATs focuses on the aerodynamic optimization of the turbine, however, the development and production of commercial RATs is carried out mainly by companies (Xia et al., 2018), it is assumed much information is undisclosed, hence this literature survey focuses on information in the public domain, like studies on HAWT.

The wind turbine extracts energy from the moving air and thus slows it down. In other words, the wind turbine acts opposite than a propeller which accelerates the air as relatives to the aircraft, i.e., puts energy into the air and the aircraft gains thrust. Hence, for the turbine the aircraft will gain further drag due to the RAT. The thrust acting on the turbine is noted by  $T$  and the coefficient of thrust of the turbine is defined by equation 2.1. Fig. 2.3 shows the decomposition of thrust force along the rotor axis.

$$C_T = \frac{T}{\frac{1}{2}\rho AV^2} \quad (2.1)$$

Where  $\rho$  is the density,  $A$  is the swept area of the rotor blades and  $V$  is the wind speed.

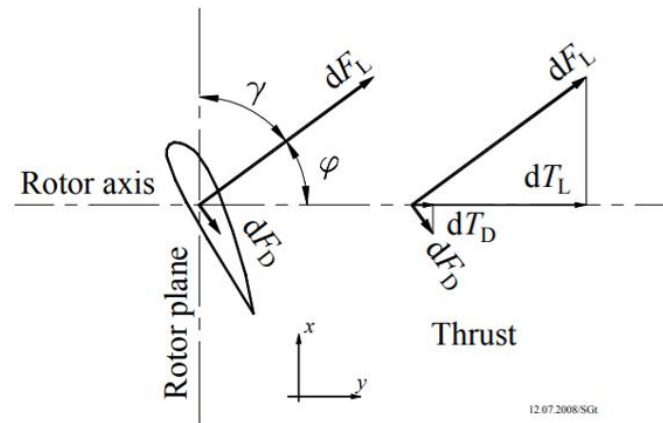


**Figure 2.3.** Thrust force decomposed along the rotor axis (Gundtoft, 2009).

In terrestrial turbines, the drag acting on the turbine is mostly important due to structural consideration of the blades and the pillar. For example, in the horizontal axis wind turbine (HAWT) the blades bend due to the drag and hit the pillar for a forward-facing rotor (i.e. the pillar is behind the rotor). This caused earlier terrestrial HAWT that had backwards faced rotor (i.e. the pillar is upstream the rotor), to have a reduction in the turbine's power output due to the turbine wake in the pillar.

In case of the RAT,  $T$  or  $C_T$  get extra importance, it will increase the aircraft drag and slow it down (unless the engine thrust increases to compensate). Furthermore, the power gained from the turbine will always be smaller than the power needed from the engine to keep the aircraft at the same speed. This is truly expressed in the limit of BETZ of  $C_P < 16/27$ . Hence the need to consider  $C_T$  is highly important for the RAT, this and the other parameters are closely examined in this study.

## 2.1 Wind turbines

Wind energy is one of the most common ways of obtaining clean and sustainable energy. Because of their characteristics of being practical and economic, its role has become important in renewable energy. Wind turbines extract energy from the motion of wind available (Sahin 2004). Wind energy has been used for at least 3000 years (Sahin, 2004) and has the advantage that its main resource is wind, and it is a non-limited resource on earth. A mayor disadvantage for wind turbines in the inability to store the energy for later use and that the energy is not persistent in time because it depends on the speed of the wind available (Manwell, 2002).

Wind turbines can be drag or lift based (or a combination of both). Drag based turbines appeared earlier in human history than lift based turbines. Drag based turbines are simpler and usually do not require minimum wind speed to start, i.e., they can be self-starting. However, for a modern aerodynamically designed body as a blade profile, the aerodynamic lift force can be much higher than the drag force turbine, and the power harnessed in lift-based turbines is much higher than in drag-based turbines, hence, in this study we focus on lift-based turbines. For simplicity we will just call them wind turbines while remembering there are lift based turbines.

Wind turbines can be classified in two categories: Horizontal Axis Wind Turbine (HAWT) (Lift based) and Vertical Axis Wind Turbine (VAWT) (drag based) (M. F. Ismail, 2014). The blades of HAWTs rotate around an axis that is parallel to the airflow (Figure 2.4) while in VAWTs (Figure 2.5), the blades rotate around an axis perpendicular to the airflow.



**Figure 2.4.** Three-blade horizontal Axis Wind Turbine (M. F. Ismail, 2014).



**Figure 2.5.** Three-blade vertical Axis Wind Turbine (M. F. Ismail, 2014).

The advantage of VAWT is that it is not sensitive to the wind direction and usually generates less noise than the HAWT (Yan, 2020). The disadvantage is a much-reduced  $C_p$  as compared to the HAWT operating at the same wind conditions. The reason is that the angle of attack on the blade changes and easily gets to high values, leading to stall and post stall conditions. The AoA changes from positive to negative and hence the use of symmetries profiles for VAWT. Also, one blade is positioned after another blade wakes, thus further reduction of aerodynamic performance. The HAWT configuration is much more suitable for the RAT as the wind direction is horizontal as long as the aircraft have yaw stability. As it can develop much higher  $C_p$  than the VAWT, RATs are on the HAWT family.

In the research carried out by Ronit K. Singh and M. Rafiuddin Ahmed, made in 2013, results of optimization of a small wind turbine operating at low speeds at the range of 3-6 m/s were presented. The improvement consisted in designing a blade to operate at low speeds, this was achieved by using a special wing profile to operate in these conditions, increasing the length of the blades by 8.26% and using a pitch angle of  $18^\circ$  (Singh & Ahmed, 2013), which is the angle of rotation of the blades regarding the longitudinal axis (Abir et al., 2017). Presented results show that the increase in the length of the blades improved the power coefficient in the three different pitch angles studied and it was found that this coefficient was higher in a 2-blade turbine than a 3-blade turbine (Singh & Ahmed, 2013). The highest power coefficient ( $C_p$ ) achieved was 0.29 at a speed of 6 m/s at a tower mounted on a pole with height of 8.22 m. On average this coefficient has a value of 0.25 in small turbines and in large turbines is 0.45 (Singh & Ahmed, 2013).

## **2.2 RAT design and analysis**

The airfoil can be described as the shape of a transversal area of an aerodynamic object such as a wing (Figure 2.6). Airfoils work with Bernoulli's principle, the pressure difference generated in the upper and lower surface of the airfoil results in lift generation. Airfoils are used on those surfaces designed to generate lift like aircraft wings and turbine blades.

Airfoils are categorized in families according to common shapes or design characteristics, one of the most well-known airfoil groups is the National Advisory Committee for Aeronautics (NACA) family developed by the U.S. government aeronautical agency (a.k.a. NASA). The airfoil families were systematically designed, subjected to testing, and their aerodynamic properties were documented (Sóbester & Forrester, 2014).

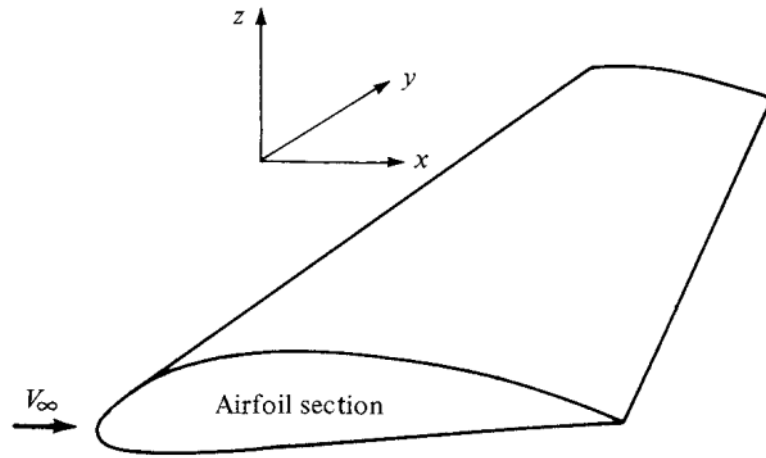


**Figure 2.6.** Airfoil section (John D. Anderson, 2012).

The key components of an airfoil are illustrated in Figure 2.7, The components that will be often referred to in this study include the Leading Edge (L.E.), Trailing Edge (T.E.) and the chord ( $c$ ). The location of the camber line, nose radius ( $r_o$ ), the maximum thickness ( $t_{max}$ ), the maximum camber ( $Z_{max}$ ) and its distance ( $X_c$ ) are also shown in Figure 2.7.

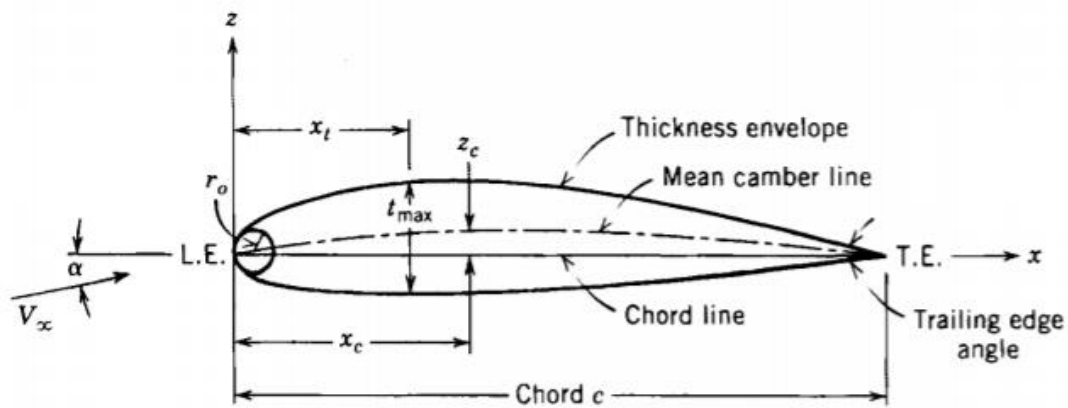


**Figure 2.7.** Geometric variables of an airfoil (Martin, 1998).

Researchers focus their attention on the following parameters when turbine optimization is sought: (1) Energy production maximization, (2) energy cost reduction and (3) blade turbine mass reduction (Sharma et al., 2021). In this study, we focus on the first parameter, that can be translated to turbine's  $C_p$  increase. The blade performance of the turbine directly affects the RAT's efficiency (X. Zhang et al., 2018). Thus, one of the main

focuses in RAT optimization is the enhancement of the aerodynamic performance on the blades, this can be achieved through out a series of modifications in blade's profile.

Numerical simulation approach has the ability to simulate the physical behavior that the turbine will have when interacting with the airflow, due the advancement of computer technology and simulation methods (Yang & Liang, 2010). There are a variety of optimization methods that can be applied to HAWT. Sharma et al. (2021) reviewed a variety of methods used by researchers for airfoil optimization on wind turbine blades. Parameterization, Genetic Algorithms, CFD and Adjoint methods among other approaches are reviewed in the article (Sharma et al., 2021). In this study, the CFD as well as the BEM method will be extensively used to analyze the performance of the RAT.

CFD method consists of solving Reynolds Average Navier Stokes (RANS) equations to predict the behavior of fluids around an object. When performing a CFD analysis a few parameters need to be taking into account like the domain size and shape of the geometry to analyze, the grid generation and the turbulence model. A C-type grid is identified by its inlet in shape of a "C", leading to a rectangular outlet. This grid type has been extensively adopted in studies from Syawitri et al. (2022), Aksoy (2020) and Yan Y.(2020) because it offers good accuracy and reduce computational cost in comparison to a rectangular grid.

The Blade Element Momentum Theory (BEM) consists of the assumption that, along span wise direction, the blade can be studied as a set of independent elements (ElQatary & Elhadidi, 2013). The same method has been applied to the RATs. Wang et al. (2015) implemented BEM theory to design two airfoils which performance was studied at incoming Mach number of 0.5 and 0.55. In this research, the different properties of the RAT blades using CFD method were also analyzed. The experiment consisted of the study of the aerodynamic performance of two types of blades under two different operating conditions. The common features of these two airfoils are that they have a thin profile with a large camber and both airfoils have a high lift coefficient when the angle of attack is small, allowing them to operate in a wider range of conditions.

Wang et al. (2015) establish that when the RAT's operating condition is known, the tip-speed ratio of each blade section can be calculated, allowing the flow angle of each cross

section to be determined. This paper reveals that rotors with low pitch angle generate a greater initial Thrust due to the high lift experienced in different sections of the blade created because blades have torsion. The Thrust decreases rapidly as the blade pitch angle increases above  $20^\circ$  as stall starts to occur (J. Wang et al., 2015). Guo et al. suggest that low pitch angle of the blades result in a larger power coefficient (X. Zhang et al., 2018).

Although BEM theory is commonly used for wind turbine performance calculation (Yang & Liang, 2010), there are other applicable theories for RATs performance calculation. In 2014, Renganathan et al. employed the Lift Line Theory method of Prandtl instead of the BEM theory. LL theory has been used in the conceptual design of rotors for many years. In this study, a blade was divided into six sections, which would be analyzed by employing the OVERFLOW code based on LL theory equations. In the LL analysis, the aerodynamic coefficients are in a function of local flow conditions such as the Reynolds and Mach number and the angle of attack at the blade section. In order to obtain the aerodynamic coefficients along the blade span, the aerodynamic properties are lineally interpolated in the six blade sections during the CFD analysis. The data obtained in this paper shows that LL theory can predict power output of the RAT in the range of  $M= 0-0.8$  within 20% and estimate the turbine pitch variations within 10% regarding to experimental data (Figure 2.8 and Figure 2.9).

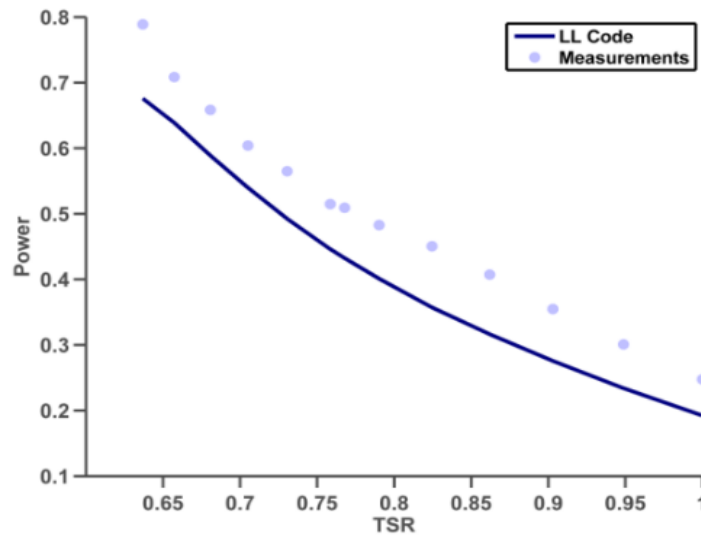


**Figure 2.8.** Comparison of LL code prediction and experimental measure of RAT power at  $M < 0.6$  (Renganathan et al., 2014).

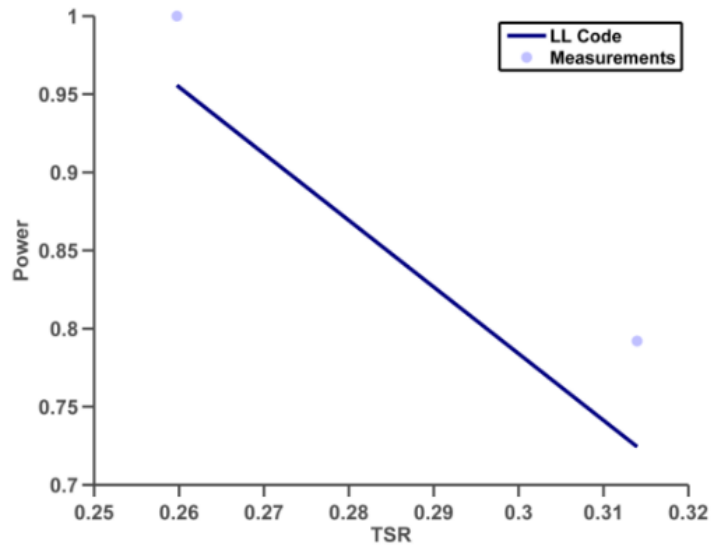


**Figure 2.9.** Comparison of LL code prediction and experimental measure of RAT power, at  $0.6 < M < 0.8$  (Renganathan et al., 2014).

On Renganathan et al. (2014) study, it was determined that high lift coefficients result in a thin blade design which has low efficiency at high speeds, but high efficiency at low speeds. Otherwise, low lift coefficients result in a wide blade design which generates a considerable amount of drag at high speeds (Renganathan et al., 2014). As mentioned before, the drag in the RAT turbine (CT) is ideally low, while maintaining a high  $C_P$  (Akagi, 2021).

### 2.3 Operating conditions study

Walter M. y Mavris D. N. (2016) focused on studied RAT's blade properties under different operating conditions. The optimization method employed is based on sequential sampling that guides the optimization process with the objective of achieving a robust RAT design whose performance was not much affected by the variation on the operating conditions.

In research performed by Wang Jian (2016), the performance of a RAT at high and low altitudes was studied by implementing the CFD method, to analyze the correlation between these two operating conditions and provide reference data for further studies on RAT designs. N.S Tachos et al. (2009) also implemented the CFD method to calculate the aerodynamic performance of a RAT rotor comparison of the data obtained implementing the

CFD method and the data obtained experimentally in a wind tunnel shows that CFD codes can accurately predict the aerodynamic characteristics of the RAT's rotor.

Turbulence models are a set of equations that make it possible for the CFD software to predict the fluid behavior. The turbulence models used in this work are derived from the Reynolds averaged Navier Stokes equations. The Spalart-Allmaras (S-A) model is one equation turbulence models, and it is known for its simplicity and computational efficiency. On the other hand, the  $k - \omega$  and  $k - \epsilon$  models solve for two equations, the former is good predicting the flow near the wall and the latter performs better on free-stream flows. Shear Stress Transport (SST) –  $k$  model combines elements from both  $k - \omega$  and  $k - \epsilon$  models, making it suitable for a wide range of flows.

In Wang Jiang's (2016) study, three turbulence models (model SST  $k - \omega$ ,  $k - \epsilon$  y S-A) were compared with test data in order to determine the optimal model to be used in the investigation. Results obtained for the three models were similar to the test data, which indicated the reliance and validation of them. However, results obtained when implemented SST  $k - \omega$  model, are the closest to test data, therefore this last model was selected to carry out the investigation.

In Wang Jiang's (2016) paper, highlighted three similarity criteria about low and high altitudes, these criteria were Reynolds number similarity, Mach number similarity and dynamic pressure similarity. According to the results obtained, no matter which similarity criteria were adopted, there was no evidence that the dimensional quantities (Thrust, power, etc.) on the ground correspond to the dimensional quantities at a high altitude. But adopting the Mach number similarity criteria, achieved that the dimensionless coefficients (Thrust coefficient, power coefficient, etc.) on the ground correspond to the dimensionless coefficients at high altitude.

From the selected literature it is sought to analyze the behavior of the RAT's blades under different operating conditions with the aim of obtaining an optimized design, since they are a key element in the turbine design. In the listed bibliography, the researchers chose to implement the turbulence model SST  $k - \omega$ , where studies have shown this model was useful to obtain the aerodynamic coefficients.

## 2.4 Gurney flaps

The Gurney flap is a surface control device used to enhance the aerodynamic properties of the flow around the airfoil. It was invented in 1960s by Dan Gurney with the purpose of increasing the aerodynamic efficiency on a race car (J.J. Wang et al., 2007). This flow control device is mounted in the trailing edge of the airfoil and typically has a height of 1 to 5% of the chord length of the airfoil (Li et al., 2002). GF has been widely used to enhance the aerodynamic performance of wind turbines. In Yan et al.(2020a), it was observed that besides increasing the Lift, the addition of a GF also delayed the stall in VAWT.

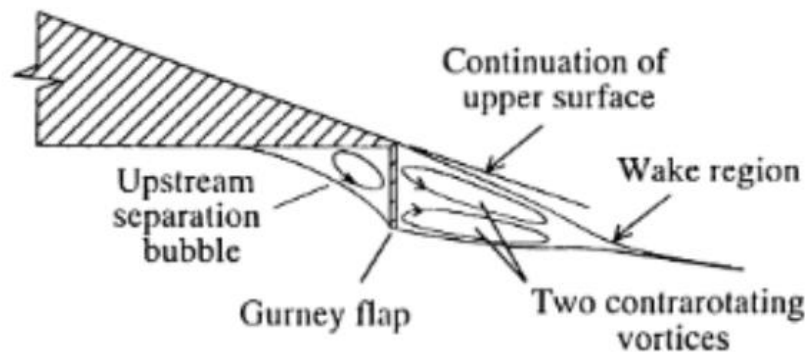


**Figure 2.10.** Gurney Flap (Jang et al., 1998).

The Gurney Flap (Figure 2.10) creates an alteration of the flow around the airfoil increasing the pressure in the upper surface of the airfoil and helps the delay of flow separation.

Numerous experimental tests conducted in wind tunnels and through computational simulations have explored the impact of Gurney flaps of varying lengths on airfoils. These investigations have consistently revealed that this device can considerably enhance the performance of an airfoil. Studies show that the GF height increase is related to the raise of  $C_L$  and  $C_D$ , in Wang et al. (2007) it was demonstrated that the  $C_D$  will rapidly raise when the GF height exceeds 2% $c$ .

The GF devices applied in VAWT as well as in HAWT help to improve the turbine efficiency. In Syawitri et al. (2022) work, it was shown that the addition of GF in a VAWT improved the  $C_P$  at low TSR range. Zhang et al. (2019), added a GF along the blade,

extending from the root to the mid-span section. The GF height was 1% c with a width of 0.15% c. This resulted in an increase in the  $C_P$  of the rotor by 21% at a TSR=6.35.

In 2002, Li et al. conducted wind tunnel test experiments on a NACA 0012 airfoil at a Reynolds number of  $2 \times 10^6$ . They observed an increase of  $C_L/C_D$  ratio by 10 times when  $C_L$  was greater than 1.0 using a GF of 0.5%c. According to experimental results conducted on a S903 airfoil (Maughmer & Bramesfeld, 2008), the GF of 2%c height, achieves a significant 29% increase in the maximum  $C_L$  compared to the clean airfoil.

CFD analysis was conducted on a NACA 0018 airfoil to examine the effects of various GF heights. The results showed that using GF heights of %1c, %2c, %3c, %4c, and %5c resulted in an increase of 16.5%, 28.7%, 39.5%, and 48.8% in  $C_L$ , respectively. Furthermore, it was observed that the GF height of 2%c corresponded to the highest  $C_L/C_D$  ratio within the AoA range of  $5^\circ$  to  $12^\circ$  (Yan, 2020).

## Chapter 3

### 3. Computational methodology

#### 3.1 Introduction

Two types of computational methodology were used in this study. The computational methods are the Reynolds-Averaged Navier Stokes (RANS) solvers and the blade element momentum (BEM) method.

The RANS equations represent a set of partial differential equations derived from the fundamental conservation laws of mass, momentum, and energy. These equations provide an Eulerian description of fluid flow, capturing the mean flow behavior by averaging over time. By solving the RANS equations, it is possible to obtain information of the flow patterns, pressure distribution, and forces acting on solid bodies immersed in the fluid. In this study, the RANS equations are employed to study the aerodynamic behavior and performance of the NACA 8318 airfoil, aiding in the design and optimization of a rotor of the RAT.

Through this research, the software ANSYS Fluent was used to calculate turbulent flow characteristics. The RANS approach requires models of turbulence effect on the mean flow, such as the eddy viscosity and turbulent stresses models. The turbulence models like the Shear Stress Transport (SST) and the k-epsilon model, are commonly used for RANS computations for external and internal flows. In this project we used the k- $\omega$  and the SST variant as described later.

In addition to the RANS equations, the Blade Element Momentum (BEM) method is a numerical technique to study the aerodynamics performance of rotors as of RAT. In this study the software Qblade, which implements the BEM method, was used to obtain the power, and thrust coefficient of the RAT's rotor. The BEM method consists of dividing a rotor blade into multiple sections, referred to as blade elements. Each element is treated as a discrete lifting surface, and the flow around it is approximated using 2D aerodynamic model and empirical data. The BEM method is much faster than a 3D CFD for the RAT rotor and thus was heavily used in this study.

Throughout this chapter, we will introduce the RANS equations, turbulence models, and the BEM method in the context of fluid flow analysis. The RANS method is to be used to study 2D aerodynamics and the BEM method is to be used to study the RAT's rotor where the aerodynamic performance of the blade is taken from 2D CFD.

### 3.2 Governing equations

The Navier stokes equations are derived from basic physics laws: Conservation of mass, the momentum and energy (White, 2011). There are two different approaches to look at the fluid flow, Eulerian and Lagrangian. We use the commonly employed fluid flow Eulerian approach where the flow is assumed as continuous of unsteady control volume.

Equation (3.1) represents the Conservation of mass, also known as continuity relation, for an infinitesimal control volume in rectangular coordinates (White, 2011):

$$\frac{\partial \rho}{\partial t} + \frac{\partial}{\partial x}(\rho u) + \frac{\partial}{\partial y}(\rho v) + \frac{\partial}{\partial z}(\rho w) = 0 \quad (3.1)$$

Where  $\rho$  refers to the fluid density and  $t$  is time. The velocity component is denoted by  $u$ ,  $v$  and  $w$  in the directions of  $x$ ,  $y$  and  $z$  respectively. Using tensor notation, the continuity equation can be written as shown in equation (3.2) (Andersson et al., 2011).

$$\frac{\partial \rho}{\partial t} + \frac{\partial \rho u_i}{\partial x_i} = 0 \quad (3.2)$$

For incompressible flows regardless of if the flow is steady or not, the variation of density with time will be equal to zero  $\frac{\partial \rho}{\partial t} = 0$ , leading to equation (3.3). One should note that for stratified flows in the ocean  $\frac{D\rho}{Dt} = 0$  i.e.,  $\frac{\partial \rho}{\partial t} + \frac{\partial \rho u_i}{\partial x_i} = 0$ . However, in the case of the RAT, as long as  $M < 0.3$ , we can assume that  $\rho$  is constant and the flow is incompressible.

$$\frac{\partial u_i}{\partial x_i} = 0 \quad (3.3)$$

The momentum equation, often known as the Navier Stokes equation, is presented in eq. (3.4), where, for incompressible flows we can also assume that density is constant therefore the momentum for incompressible flows is expressed in eq. (3.5).

$$\frac{\partial \rho u_i}{\partial t} + \frac{\partial \rho u_i u_j}{\partial x_j} = -\frac{\partial p}{\partial x_i} + \frac{\partial \tau_{ij}}{\partial x_j} + \rho g_i \quad (3.4)$$

$$\frac{\partial \rho u_i}{\partial t} + \frac{\partial \rho u_i u_j}{\partial x_j} = -\frac{\partial p}{\partial x_i} + \frac{\partial \tau_{ij}}{\partial x_j} \quad (3.5)$$

For the Newtonian fluid, the stress tensor  $\tau_{ij}$  is proportional to the deformation speed and the viscous coefficient. For incompressible flow ( $M < 0.3$ ) the stress tensor is expressed as equation (3.6) (Andersson et al., 2011).

$$\tau_{ij} = \mu \left( \frac{\partial u_i}{\partial x_j} + \frac{\partial u_j}{\partial x_i} \right) \quad (3.6)$$

Where the dynamic viscosity  $\mu$  is assumed to be constant. For ideal gas it depends on the temperature, and we assume the temperature does not much change for  $M < 0.3$ . If compressible flow is computed, the energy equation is to be considered as well.

### 3.3 Turbulence models

When analyzing a fluid with CFD, the focus is placed on the time-averaged properties of the flow like mean velocity ( $\bar{u}_i$ ) and mean pressure ( $\bar{p}$ ). Reynolds Averaged Navier-Stokes (RANS) equations are widely employed in CFD to simulate and analyze turbulence flows. These equations focus on the mean properties of the flow, are time-average and are classified according to the number of extra transport equations that are added (Versteeg, 1995).

The RANS equations solve for  $\bar{p}$  and  $\bar{u}_i$ , where the bar denotes time averaged. Following this, the velocity equation can be expressed as:

$$u_i = \bar{u}_i + u_i' \quad (3.7)$$

Where the prime denotes the fluctuating component. Hence the time-averaged convection term in equation (3.5) is:

$$\overline{u_i u_j} = \bar{u}_i \bar{u}_j + \overline{u'_i u'_j} \quad (3.8)$$

Where the fluctuating term  $(\overline{u'_i u'_j})$  is known as the Reynolds stress ( $R_{ij}$ ) that needs to be modeled. Hence the RANS equation for incompressible flow is:

$$\frac{\partial \rho \bar{u}_i}{\partial t} + \frac{\partial \rho \bar{u}_i \bar{u}_j}{\partial x_j} = -\frac{\partial \bar{p}}{\partial x_i} + \frac{\partial}{\partial x_j} (2\mu S_{ij} - \overline{u'_i u'_j}) \quad (3.9)$$

Where the strain tensor is  $S_{ij} = \frac{1}{2} \left( \frac{\partial \bar{u}_i}{\partial x_j} + \frac{\partial \bar{u}_j}{\partial x_i} \right)$ .

### 3.3.1 Model k – $\omega$

The k –  $\omega$  model, developed by David Wilcox, is good at predicting turbulence near the wall at low Reynolds number. This two-equation model solves for the turbulent kinetic energy ( $\kappa$ ) and its dissipation rate ( $\omega$ ) (Dewan, 1967). The transport equations for  $\kappa$  and  $\omega$  are expressed in equation (3.10) and (3.11), respectively.

$$\frac{\partial k}{\partial t} + \bar{u}_j \frac{\partial k}{\partial x_j} = \frac{\partial}{\partial x_j} \left[ \left( \nu + \sigma^* \frac{\kappa}{\omega} \right) \frac{\partial k}{\partial x_j} \right] + \tau_{ij} \frac{\partial \bar{u}_i}{\partial x_j} - \beta^* k \omega \quad (3.10)$$

$$\frac{\partial \omega}{\partial t} + \bar{u}_j \frac{\partial \omega}{\partial x_j} = \frac{\partial}{\partial x_j} \left[ \left( \nu + \sigma \frac{\kappa}{\omega} \right) \frac{\partial \omega}{\partial x_j} \right] + \alpha \frac{\omega}{\kappa} \tau_{ij} \frac{\partial \bar{u}_i}{\partial x_j} - \beta \omega^2 \quad (3.11)$$

Where  $\alpha, \beta, \beta^*, \sigma$  and  $\sigma^*$  are constants:

$$\alpha = \frac{5}{9}, \quad \beta = \frac{3}{40}, \quad \beta^* = \frac{9}{100}, \quad \sigma = \frac{1}{2}, \quad \sigma^* = \frac{1}{2}$$

the turbulent eddy viscosity ( $\nu_T$ ) is:

$$v_T = \frac{\kappa}{\omega} \quad (3.12)$$

and Kinematic viscosity is calculated from:

$$v = \frac{\mu}{\rho} \quad (3.13)$$

### 3.3.2 Model SST k – $\omega$

The Shear Stress Transport (SST) k –  $\omega$  model, introduced by Menter, is an improved version of k –  $\omega$ . This model incorporates the benefits of accurately predicting near-wall flow behavior from the k –  $\omega$  model with the capability to provide precise results for far field flows from the k –  $\epsilon$  model (L. Wang et al., 2016).

The transport equations for  $\kappa$  y  $\omega$  are (Dewan, 1967):

$$\frac{\partial k}{\partial t} + \bar{u}_j \frac{\partial k}{\partial x_j} = \frac{\partial}{\partial x_j} \left[ (v + \sigma_k v_t) \frac{\partial k}{\partial x_j} \right] + P_k - \beta^* k \omega \quad (3.14)$$

$$\frac{\partial \omega}{\partial t} + \bar{u}_j \frac{\partial \omega}{\partial x_j} = \frac{\gamma P_k}{\rho v_t} - \beta \omega^2 + \frac{\partial}{\partial x_j} \left[ (v + \sigma_\omega v_t) \frac{\partial \omega}{\partial x_j} \right] + 2(1 - F_1) \sigma_{\omega 2} \frac{1}{\omega} \frac{\partial k}{\partial x_j} \frac{\partial \omega}{\partial x_j} \quad (3.15)$$

Where the eddy viscosity is defined as,

$$v_T = \frac{a_1 \kappa}{\max(a_1 \omega, SF_2)} \quad (3.16)$$

Where  $a_1$  and  $F_2$  are defined in Dewan (1967).

## 3.4 Blade Element Momentum

The Blade Element Momentum (BEM) method is a widely applied technique, primarily used for wind turbine analysis. It combines the momentum and blade element theory and consists in subdividing the turbine blades into numerous elements and analyzing each of these elements separately. This approach simplifies the analysis by assuming no interaction between elements, treating each part of the blade as individual airfoils. The advantage of BEM method is that it requires minimal computational resources and delivers accurate results, however it lacks the capability to visualize the flow around the turbine. The

BEM method uses local flow conditions of the turbine and calculates the local aerodynamic forces to provide more realistic results of the rotating turbine.

Several steps need to be followed to calculate the aerodynamic forces and to obtain and optimal rotor design:

1. Discretization: The turbine is subdivided into several annular elements along the turbine radius.
2. Initialization of  $a$  and  $a'$ : The axial and tangential interference factor ( $a$  and  $a'$ ) are initialized in zero as a first guess.
3. Angle of attack: The angle of attack can be calculated with equation (3.17) where  $\theta$  is the pitch angle, which is given from the blade design.

$$\alpha = \varphi - \theta \quad (3.17)$$

The flow angle ( $\varphi$ ) can be calculated as shown in equation (3.18).

$$\tan \varphi = \frac{(1 - a) V}{(1 + a') r \omega} \quad (3.18)$$

Where  $V$  is the wind speed,  $r$  is the radial distance of the element from the hub and  $\omega$  is the angular speed in the rotor.

4. Aerodynamic coefficients: The variations of the lift and drag coefficients ( $C_L$  and  $C_D$ ) with the angle of attack are known from 2D CFD, experimental data or theory.
5. Interference factors: The interference factors  $a$  and  $a'$  are calculated using equations (3.19) and (3.20) (Gundtoft, 2009).

$$a = \frac{1}{\frac{4F \sin^2 \varphi}{\sigma C_y} + 1} \quad (3.19)$$

$$a' = \frac{1}{\frac{4F \sin \varphi \cos \varphi}{\sigma C_x} - 1} \quad (3.20)$$

Where  $C_x$  and  $C_y$  are given by equations (3.21) and (3.22).

$$C_x = C_L \sin \varphi - C_D \cos \varphi \quad (3.21)$$

$$C_y = C_L \cos \varphi + C_D \sin \varphi \quad (3.22)$$

6. Check convergence: Values of  $a$  and  $\gamma$  need to be no more than 1% different from the initial guess or last guess, if they are, then the values should be re calculated again as this is a linear iteration approach.

7. Calculate local forces on the blade. Lift and drag forces on the blade element are calculated, for further details see Hansen (2008) and (Gundtoft, 2009).

### 3.5 Computational Fluid Dynamics

Previously in the beginning of the chapter, the RANS equations were examined, now we look at the solution using Computational Fluid Dynamics (CFD). Decades of research have improved CFD approach to provide reliable prediction for complex flows (Ryu et al., 1994).

CFD provides an insight into fluid behavior around an object and allows flow visualization. It enables the evaluation of products before building physical prototypes resulting in cost savings (Andersson et al., 2011). Nowadays, CFD analysis primarily serves two key purposes: first, it aids in comprehending flow behavior and, second, it provides estimations of forces and moments (Cosner et al., 1994).

The precision of simulations varies depending on the type of flow under consideration. Single-phase laminar flows can generally be simulated with good accuracy in most situations, whereas simulations of single-phase turbulent flows, while reliable, tend to exhibit lower levels of accuracy. Modern CFD codes have the capability to model a broad spectrum of systems.

To perform a CFD analysis several steps need to be followed. Below the main steps described by Anderson et al. (2011) are shown.

- 1. Geometry modeling.** A 2D or 3D model needs to be created using Computer Aid Design (CAD) software. One should note that the domain where the geometry to analyze is immersed also needs to be modeled.
- 2. Grid generation.** This is one of the crucial steps to obtain accurate results. A proper grid size and structure need to be selected.

3. **Defining models.** CFD software contains a variety of models for different types of flows, in this study turbulence models were employed to analyze turbulence flow.
4. **Set properties.** The properties of the fluid such as density, temperature and viscosity are defined in this phase.
5. **Set boundaries and inlet conditions.** In this phase, the information about the fluid interaction with the surface is provided by setting inlet, outlet, and wall conditions.
6. **Solve.** In this step the solver type, the convergence criteria, and the iteration method are defined. These parameters will affect the accuracy of the solution. The numerical discretization is important. For the diffusion (viscous) term, a central scheme is always chosen. For the convective term, it is advised to use up wind schemes for numerical stability, preferably at least second order. The formulation is commonly based on the finite volume approach.
7. **Post processing.** In the postprocessing phase, the results are analyzed to obtain information about the flow and evaluate the quality of the solution. It provides information about the flow, flow pattern, temperatures, and velocities.

### 3.6 Ram power

The maximum theoretical ram power ( $P_{th}$ ) which is the type of power extracted by the RAT from the wind stream, expressed in Watts, is proportional to the cube of air speed ( $V$ ) in m/s, the swept area ( $A$ ) of the turbine in  $m^2$  and density of the air  $\rho$  in  $kg/m^3$  as described in equation (3.23) (Xia et al., 2018).

$$P_{th} = 0.5\rho AV^3 \quad (3.23)$$

However, one should note that the power that is actually extracted by the turbine is written as  $\underline{P} = C_p P_{th}$ , where  $C_p$  is the power coefficient. The BEM method will be employed to compute  $C_p$  in this study.

### 3.7 Power coefficient

The  $C_p$  is a dimensionless number that represents the relation between the actual power and the maximum theoretical power extracted from the wind. Its value depends on the turbine

geometry, and operational speed, hence the  $C_P$  is unique depending on the turbine type. Accounting for aerodynamic losses and wake effects, the  $C_P$  has a maximum value of 16/27, this value is known as the BETZ limit. The  $C_P$  can be written as:

$$C_P = \frac{P}{0.5\rho AV^3} \quad (3.24)$$

### 3.8 Aerodynamic coefficients

The dimensionless aerodynamics coefficients are used to characterize the turbine blades and are helpful to simplify the study of its aerodynamics. In this section we will differentiate between 2D and 3D bodies, where  $C_L'$  and  $C_D'$  are the Lift and Drag coefficient for a 2D body and  $C_L$  and  $C_D$  of a 3D body.

#### 3.8.1 Lift coefficient

The lift coefficient represents the relation of the lift force applied on a body with the fluid properties and the body geometry, this force is given by equation (3.25) (John D. Anderson, 2012).

$$C_L = \frac{L}{q_\alpha S} \quad (3.25)$$

Where  $q_\alpha = \frac{1}{2}\rho V^2$  represents the dynamic pressure [Pa],  $S$  is the reference area [m<sup>2</sup>] and  $L$  is the lift force [N].

For a 2D body the  $C_L'$  is described as:

$$C_L' = \frac{L}{q_\alpha C} \quad (3.26)$$

Where  $C$  is the airfoil chord length (Distance between the leading and trailing edge) in meters.

### 3.8.2 Drag coefficient

The drag force ( $D$ ) represents the resistance of an object when it moves throughout a fluid and is generated due the friction between the fluid and the object. Its dimensionless coefficient, expressed as  $C_D$ , for a 3D body is expressed in equation (3.27), while the  $C_D'$  for a two-dimensional body is shown in equation (3.28).

$$C_D = \frac{D}{q_\alpha S} \quad (3.27)$$

$$C_D' = \frac{D}{q_\alpha C} \quad (3.28)$$

## 3.9 Turbine blades

A RAT turbine belongs to the HAWT category, these turbines are sensitive to changes made to the airfoil of the blades and their design. In this section, the most relevant parameters to be considered in the design of RAT blades are discussed.

### 3.9.1 Tip speed ratio

One of the features of a turbine blade is the tip speed ratio ( $TSR$ ), this parameter relates how fast the tip of the turbine's blades move compared to the wind speed. The  $TSR$  can be written as equation (3.29) where  $\omega$  represents the turbine rotational speed in radians per second and  $R$  the radius of the blade in meters.

$$TSR = \frac{\omega R}{V} \quad (3.29)$$

The  $TSR$  is inversely proportional to the wind speed, hence a low tip speed ratio indicates that the turbine is operating at a high speed and vice versa. In an ideal horizontal axis wind turbine with wake rotation, a large tip speed ratio is preferred, because it results with a larger power coefficient theoretically.

When selecting the appropriate tip speed ratio, several factors come into play. These factors encompass the turbine's efficiency, Thrust, mechanical load, aerodynamics, and noise

characteristics(Schubel & Crossley, 2012). One should also consider the effect on the turbines coefficient of thrust written as:

$$C_T = \frac{T}{q_\alpha} \quad (3.30)$$

### 3.9.2 Shape and quantity of the blade

A turbine blade consists of 3 regions, the root, mid span, and the tip. Figure 3,1 shows the typical shape of the turbine blade, and it also shows the location of the chord length. This typical shape is derived through optimization procedures based on the BEM approach (Hansen, 2008).

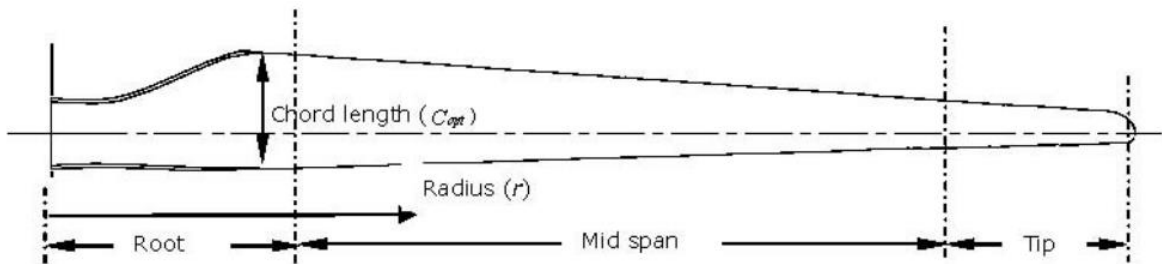


**Figure 3.1.** Typical shape of a turbine blade and the classification of its regions (Schubel & Crossley, 2012).

When designing a rotor, it is considered that a lower number of blades would decrease the weight and manufacturing costs, one should note the rotor design should also consider operational conditions at which the turbine will be functioning. In this study we are working with a two-bladed rotor employed for commercial aircraft with a constant chord length along the blade.

### **3.10 Summary**

This chapter introduced the key concepts of the Reynolds-Averaged Navier-Stokes (RANS) equations, turbulence models, and the Blade Element Momentum (BEM) method for analyzing rotor blades aerodynamics. The RANS equations help us to compute turbulent time-averaged flow patterns and forces acting on an object that is in interaction with a fluid. Turbulence models are required to close the RANS momentum equations. The BEM provides a fast method to compute the power and thrust of a rotor once its geometry is known and the 2D aerodynamic coefficients of the blade's profiles. These concepts form the computational methodology in this project.

## Chapter 4

### 4. Analysis and experimentation for problem solving.

#### 4.1 Introduction

In this chapter, 2D Computational Fluid Dynamics (CFD) is used to study the effects of adding Gurney flaps at three different height configurations of 1%, 3%, and 5% of the chord length ( $c$ ), in the NACA 8318 airfoil within a Reynolds number range spanning from 200k to 500k at blade sections of 25%, 50%, 75% and 100%. The chapter commences with an exposition of the two-dimensional CFD methodology employed for the analysis and provides an overview of the aerodynamic performance of the four airfoil configurations (clean and the three configurations with GF) studied as well as the pressure distribution along the chord line.

Results validations are presented at section 4.2.8, which contains the comparison of CFD results for the NACA 8318 airfoil at a Reynolds number of 500k, against experimental data collected by Yoshida (2000) using a rectangular wing with dimensions of 0.35m chord and 2m span. In Section 4.3, a 2D CFD analysis is conducted on the E387 airfoil, with results being validated against experimental data acquired by Shen (2016) from low-speed wind tunnel tests at a Reynolds number of 100k.

Section 4.4 is dedicated to the application of Blade Element Momentum (BEM) method to the entire turbine in Qblade software. Results obtained from 2D CFD at blade sections of 25%, 50%, 75% and 100% were used to provide accurate aerodynamic coefficients at each section of the turbine's blade designed in Qblade. This section presents a comparison of the coefficient of power ( $C_P$ ) to coefficient of thrust ( $C_T$ ) ratios for the three blades equipped with Gurney Flaps, compared with the original blade. In addition, section 4.4.1 demonstrates an analysis of these blades with GF mounted on either at the tip or at the root of the blade, examining the  $C_P/C_T$  data with Gurney Flaps in this region and contrasting it with the corresponding result for the unmodified blade.

Finally, section 4.5 summarizes the key findings and insights from the preceding sections, providing a cohesive overview of the impact of Gurney Flaps on the turbine performance.

## **4.2 NACA 8318 Computational**

In this section, a 2D analysis was conducted on the NACA 8318 airfoil for sections at 25%, 50%, 75%, and 100% of the blade, exploring a range of Angles of Attack (AoA) from 0 to 12 degrees. The analysis goes beyond considering just the operational speed of the aircraft; it accounts for the diverse speeds encountered by different sections of the turbine blade as shown in Table 4.5. As the turbine rotates, the blade tips experience higher speeds, potentially inducing compressible effects. For simplicity, this study disregarded compressibility effects, as the flow predominantly operated within the low to moderate Mach number range. To accurately simulate these conditions, the CFD analysis incorporates the varied speeds experienced by each individual blade element. Subsequently, in section 4.4, we imported the acquired data into QBlade software to determine the overall turbine efficiency. Utilizing a 2D computational analysis offered advantages such as reduced computational resource requirements and enhanced time efficiency. Additionally, it allowed for a detailed examination of airflow behavior around individual blade sections. Overall, the 2D computational analysis provided valuable insights into the aerodynamic forces of the blade sections while working within limitations of computational resources.

### **4.2.1 Initial turbine specifications**

The initial RAT geometry corresponds to a RAT configuration of a commercial aircraft. The turbine's dimensions were derived from the specifications outlined in the work of M. Bolaños (2020). The turbine's nose has a diameter of 0.180 m and a height of 0.250 m. Considering the blades and nose of the rotor, the turbine has a total diameter of 1.016 m. The turbine consists of two blades with a constant chord length (0.127 m), which have a variable pitch angle along the blade, being  $8^\circ$  at the tip and  $44^\circ$  at the root of the blade. In figure 4.1 the distribution of the pitch angle along the turbine radius is plotted.

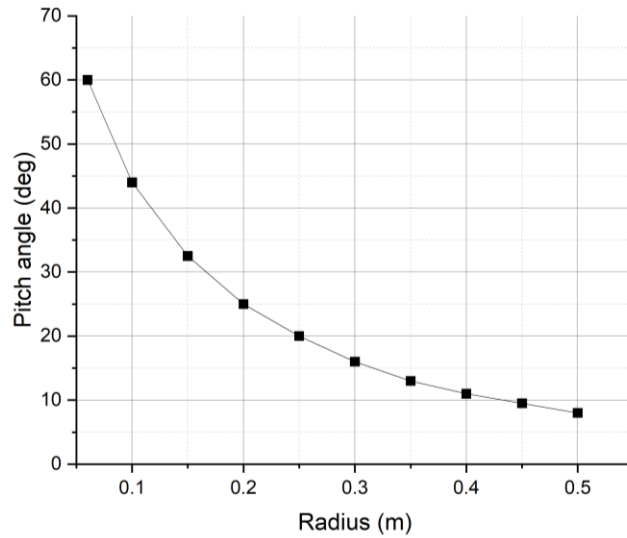


**Figure 4.1.** Pitch angle variation along the blade span in m.

### 4.2.2 Isolated airfoil

A 2D computational analysis was conducted on four blade configurations, using the NACA8318 as the base airfoil. The coordinates for the NACA 8318 profile were generated using the NACA 4-digit airfoil generator on the Airfoil Tools website, specifying a maximum camber of 8% of the chord located at 30% of the chord length, along with a thickness of 18% of the chord. The first configuration represents the original airfoil, while the remaining three configurations incorporate gurney flaps with heights of 1%, 3%, and 5% of the airfoil's chord length, as detailed in Table 4.1. These gurney flaps were positioned at a 90-degree angle at the trailing edge of the airfoil, with a chord length of 0.127 m (See figure 4.2). This follows the study of Yan (2020) for the symmetric NACA 0018 about the advantage of mounting GF at the airfoils T.E.

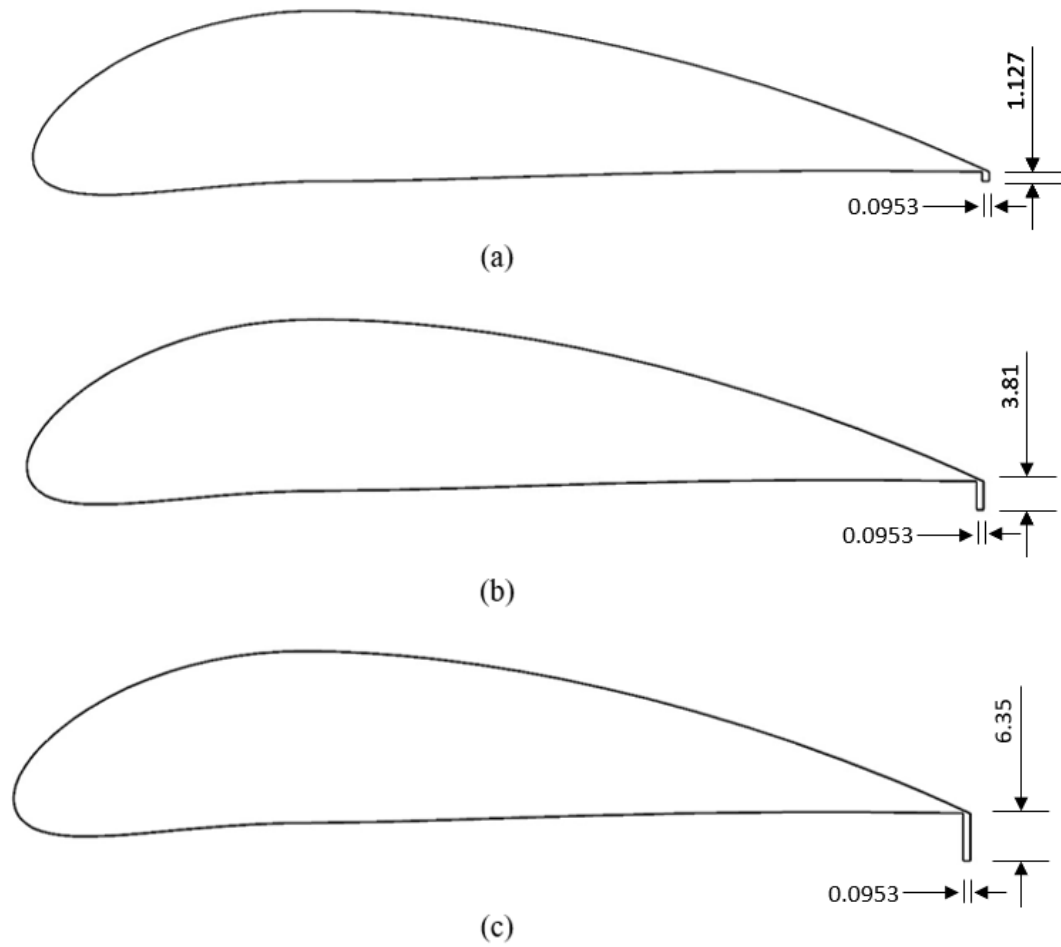


**Figure 4.2.** Airfoil with GF dimensions expressed in mm, at height configurations of (a) 1%c, (b) 3%c and (c) 5%c.

**Table 4.1.** Gurney flap dimensions.

GF configuration	Height [mm]
1%c	1.27
3%c	3.81
5%c	6.35

### 4.2.3 Operating conditions

The chosen cruising altitude was selected in consideration of historical instances of RAT application during emergency scenarios mentioned in section 1.2, where RATs were effectively deployed at altitudes around 10,000 meters. While commercial aircraft like the Boeing 757 and 767 have employed RATs at a minimum speed of 80 knots (approximately 41.16 m/s) (Saad et al., 2017), opting for 60 m/s allows us to avoid using the minimum operational condition while still maintaining a suitable margin above the required limit. The Reynolds number, which is calculated using the chord length and the velocity of the fluid in free flow, is 217,564. This value is shown in Table 4.2, additionally, the information about the atmospheric properties for the conditions studied can be found in Table 4.3. One should note that the ambient Mach of 0.175 is within the incompressible flow regimen ( $M < 0.3$ ).

**Table 4.2.** Turbine operating conditions.

Flight height [m]	10,000
Rotor angular speed [RPM]	3300
Air speed [ $\frac{m}{s}$ ]	60
Air speed [M]	0.175
Reynolds no.	217,564

**Table 4.3.** Air properties at 10,000 m (Cengel, 2006).

Altitude [m]	10000
Temperature [K]	223.25
Density [ $\frac{kg}{m^3}$ ]	0.414
Viscosity [ $\frac{kg}{m \cdot s}$ ]	$1.458e^{-5}$
Pressure [kPa]	26.5

#### 4.2.4 Computational 2D domain

The domain has a C-type shaped inlet, which helps in reducing computation time. It is situated 13 chord lengths away from the airfoil's trailing edge, with the outlet positioned 15 chord lengths downstream, as illustrated in Figure 4.3. These dimensions were chosen to ensure the accurate representation of the flow and proper flow development, resulting in accurate CFD results, the selected shape and dimensions are consistent with the findings from the literature review. The domain was created using design modeler CAD software in Ansys Workbench. The size of the domain follows the study of who investigated GF installations on the E387 airfoil.

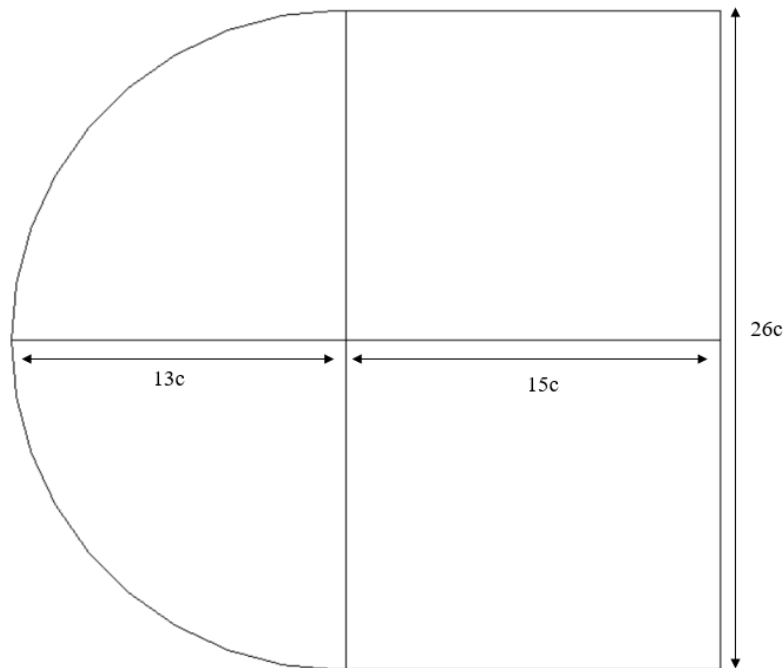


**Figure 4.3.** Dimensions of the C-type 2D computational domain based on the chord length ( $c$ ) of the airfoil. The dimensions are indicated from the point where the trailing edge of the airfoil is expected to be, extending outward to the exterior.

#### 4.2.5 Mesh generation

When performing a CFD numerical simulation, one of the most important steps is the creation of the mesh. The quality of the mesh plays a crucial role in ensuring that simulation results align closely with real-world conditions.  $Y^+$  of 1 was used due to the results of

preview mesh sensitivity tests performed for E387 and NACA 8318 at 300 k. The height of the first cell using a  $Y^+$  of 1 is actually  $1.5 \text{ e}^{-5}\text{m}$ .

**Table 4.4.** Height of first grid cell variation at different sections of the blade.

Blade section	Reynolds no.	Height of the first grid cell (m)
25%	217,530	$1.2\text{e}^{-5}$
50%	355,197	$7.8\text{e}^{-6}$
75%	507,518	$5.6\text{e}^{-6}$
100%	664,490	$4.3\text{e}^{-6}$

A C-type structured mesh was selected for the 2D domain. This mesh was refined at the boundaries of the airfoil, subdividing the airfoil section into 300 parts, as it represents the regions of interest. The vertical extent from the airfoil to the wall has been subdivided into 150 sections, while the horizontal distance from the trailing edge to the downstream area has likewise been partitioned into 150 segments. The bias function was used to refine the mesh and control the height of the initial grid cell. The bias factor varies according to the desired height of the first grid cell according to the Reynolds number of each simulation. The height of the first cell for each Reynolds number at different sections of the blade are shown in Table 4.4.

An overview of the mesh configuration for NACA 8318 clean airfoil is illustrated in Figure 4.4 and a detail section of the mesh generated for NACA 8318 airfoil with GF at 1% c is illustrated in Figure 4.5.

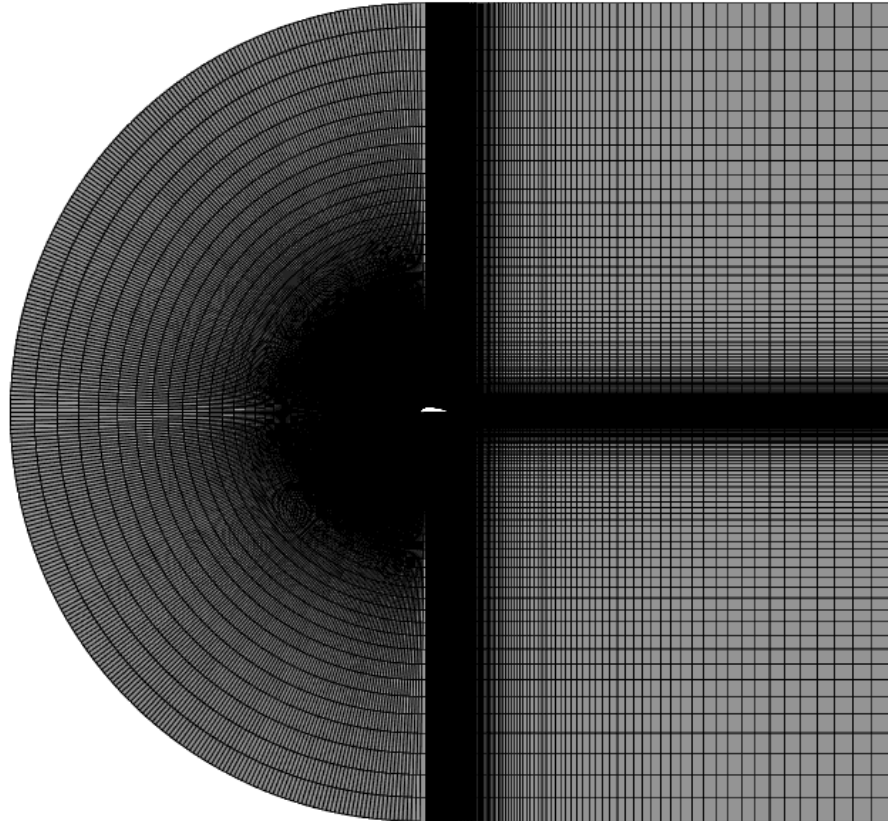


**Figure 4.4.** Overview of structured mesh for NACA 8318 airfoil.

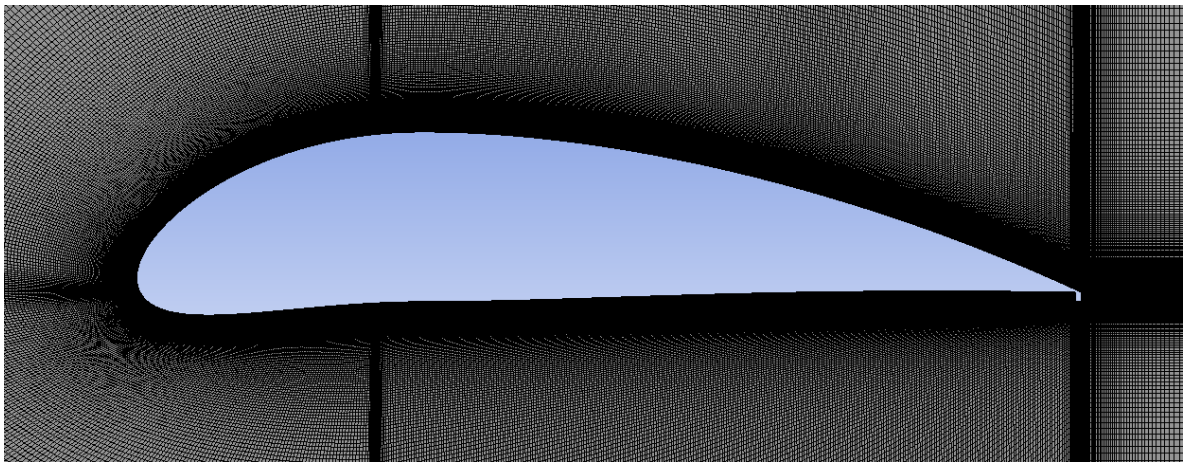


**Figure 4.5.** Detail of structured mesh for NACA 8318 with GF at 1c% airfoil.

## 4.2.6 Boundary conditions

For the 2D RANS simulation, an inlet velocity of 60 *m/s*, and the outlet pressure of 26.5 *kPa* was used according to the operational conditions shown in table 4.2. The area in the reference values was set as 0.127 *m*<sup>2</sup> and the depth as 1 *m*.

In the simulation, air properties corresponding to an altitude of 10 *km*, as detailed in Table 4.3, were employed. The value of the density used in this analysis for this condition is 0.414  $\frac{kg}{m^3}$ , the temperature is 250 *K* and the viscosity of the fluid has a value of  $1.458e^{-5} \frac{kg}{m-s}$ . The turbulent model chosen for this analysis is the *k* –  $\omega$  Shear Stress Transport (SST) model.

For turbine data, the effects of the GF were explored at each section of the blade at a range of a chord base Reynolds number of 200k to 700k accounting for the blade’s relative wind speed (*W*). The resultant speed that the blade’s section experiences can be estimated using the BEM method:

$$W^2 = (V(1 - a))^2 + (\omega r(1 + a'))^2 \quad (4.1)$$

Where *V* is the wind speed, *a* and *a'* are the axial and tangential interference factor and  $\omega$  is the angular speed in the rotor. The values of *a* and *a'* are unknown, they are dependent of the tip speed ratio (TSR). Thus, for simplicity the values of the interference factors are *a* = 1/3 and *a'*=0. The blade tangential speed at each section of the blade is shown in table 4.5.

**Table 4.5.** Velocity of the flow around the blade at blades section of 25, 50, 75 and 100%.

Blade section	Reynolds no.	Speed ( <i>m/s</i> )	Speed ( <i>M</i> )
25%	217,530	60	0.170
50%	355,198	97.950	0.280
75%	507,519	139.960	0.400
100%	664,492	183.250	0.530

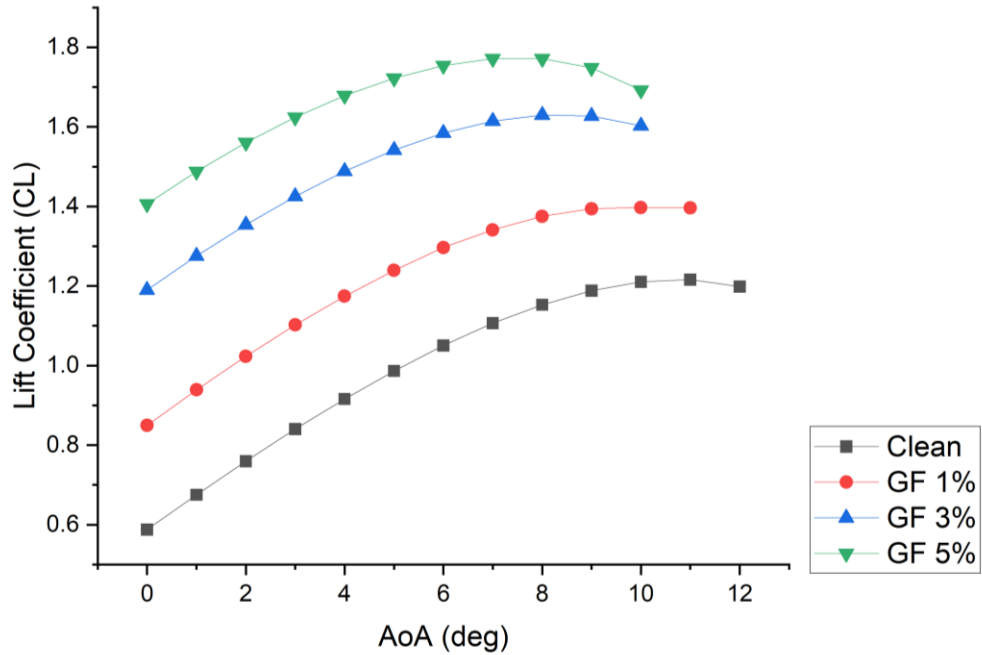
## 4.2.7 Results

In this section, the results obtained from the 2D RANS CFD simulations are presented. Figure 4.6 illustrates the relationship between Lift Coefficient ( $C_L$ ) and angle of attack (AoA), and Figure 4.7 shows the Drag Coefficient ( $C_D$ ) variation with AoA, for four distinct airfoil configurations at a Reynolds number of 217,530, corresponding to the 25% section of the blade. The term "clean" represents the airfoil configuration without a Gurney flap (GF) data, whereas the data labeled as "GF 1%, GF 3%, and GF 5%" corresponds to airfoils featuring Gurney of heights of 1%, 3%, and 5% of the airfoil chord length, respectively.

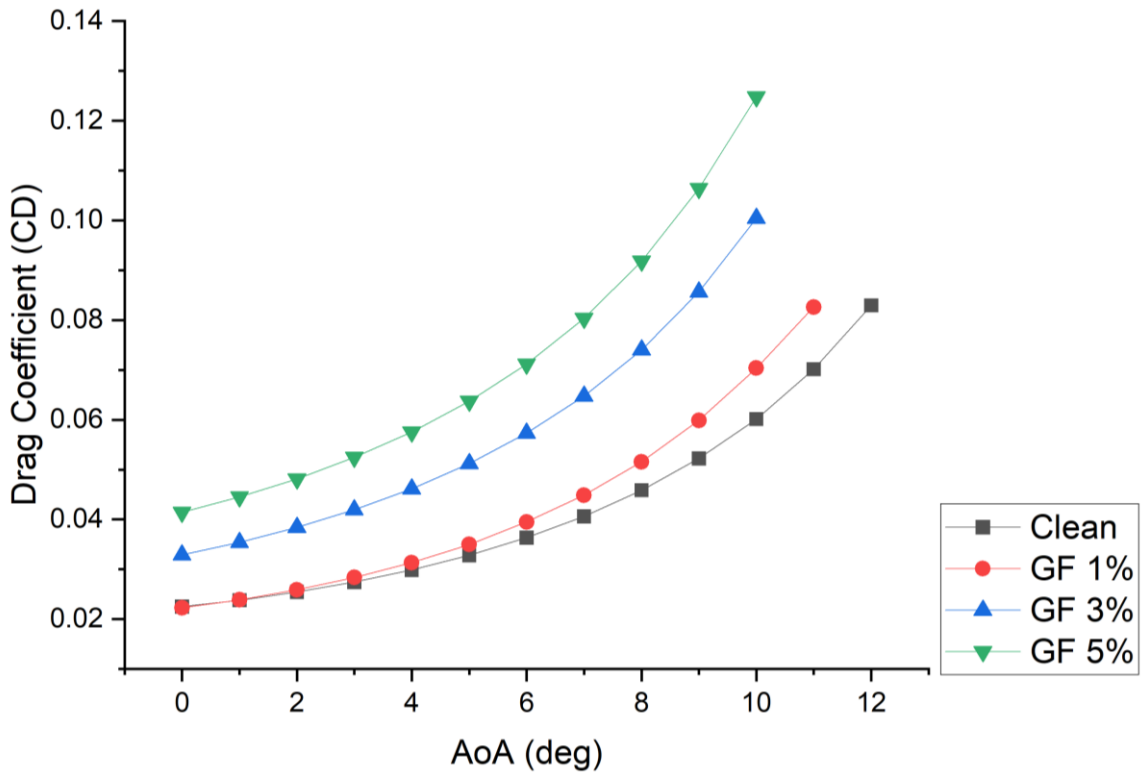
It is observed in Figure 4.6, that an increase in the Gurney flap length leads to an earlier stall, which refers to the point where a sudden reduction of the lift occurs due a separation of the flow from the airfoil, at a lower angle of attack. Furthermore, the maximum lift coefficients ( $C_L$ ) show notable variations with the use of Gurney flaps. An increment of 15.61%, 32.3%, and 43.6% in the maximum  $C_L$  values is noted, for airfoil configurations with Gurney flaps at heights of 1%, 2%, and 3% of the chord length, respectively.

The drag coefficient ( $C_D$ ) variation with the angle of attack is illustrated in Figure 4.7. The GF configuration at 1% c length exhibits a  $C_D$  behavior similar to the clean airfoil at low AoA. For GF configurations of 3%c and 5%c,  $C_D$  increases by 46% and 84% respectively at AoA=0.

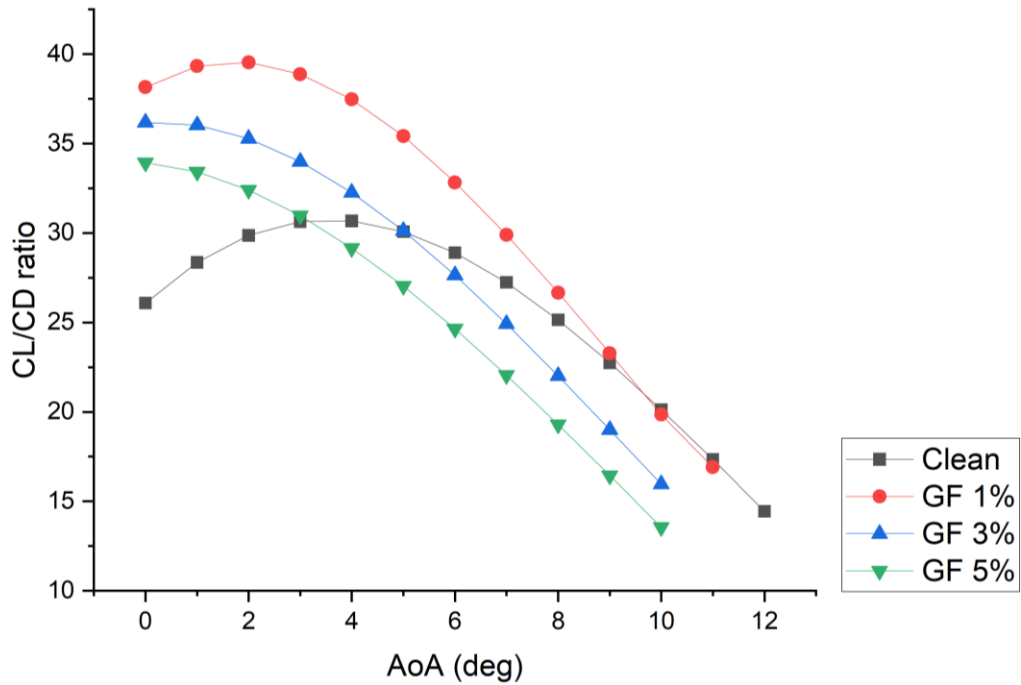
The lift to drag Ratio, which can be referred to as aerodynamic efficiency, presented in Figure 4.8, exhibits a remarkable increment at low AoA for airfoils with GF. The height of the GF is related to the reduction of the range of AoA where the  $C_L/C_D$  ratio shows improvement. This improvement is observed within AoA ranges of 0 to 9 for GF 1%c, 0 to 5 for GF 3%c and 0 to 3 degrees for GF 5%c. Furthermore, the airfoil configuration that demonstrated a consistent improvement in the  $C_L/C_D$  ratio is the GF at 1%c.



**Figure 4.6.** NACA 8318  $C_L$  vs AoA variation with GF configuration at  $Re=217,530$ .

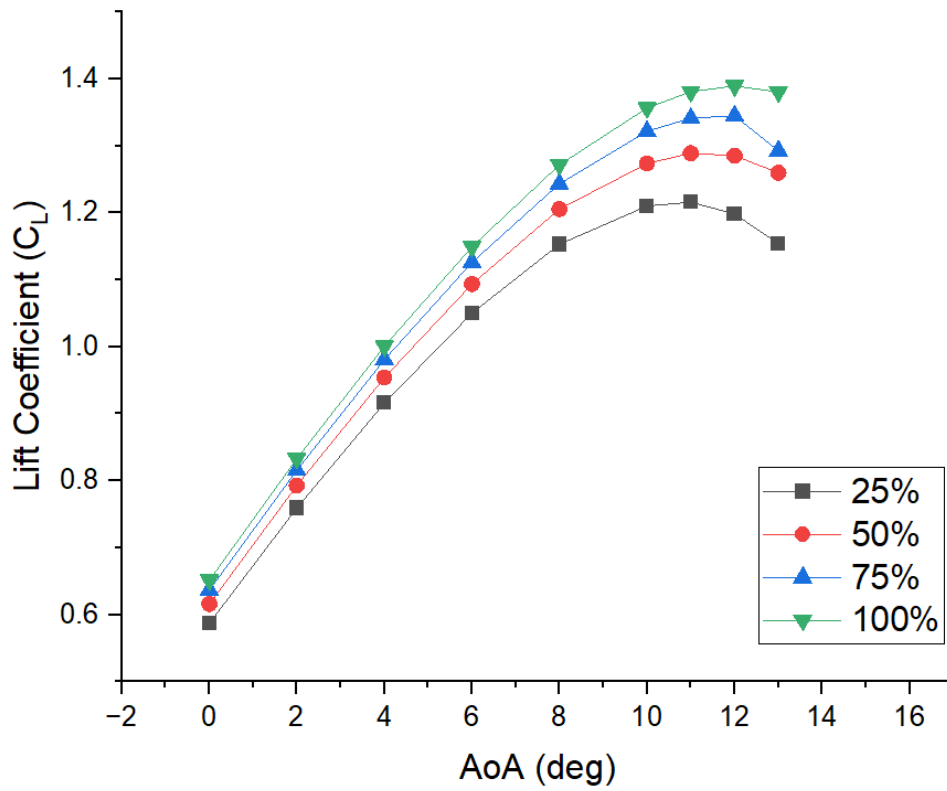


**Figure 4.7.** NACA 8318  $C_D$  variation with AoA for airfoil configurations at  $Re=217,530$ .



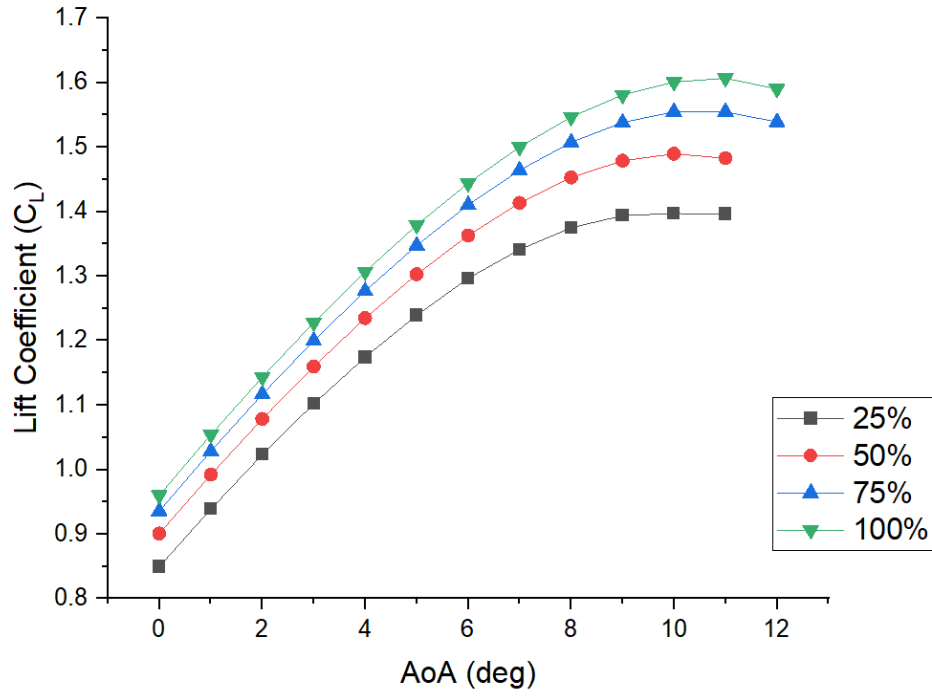
**Figure 4.8.** NACA 8318  $C_L$  to  $C_D$  ratio variation with AoA for airfoil configurations at  $Re=217,530$ .

The  $C_L$  and  $C_D$  variation with the Reynolds number for clean airfoil, and airfoils with GF at 1% and 3% are shown below. Where the 25%, 50%, 75% and 100% correspond to the section of the blade that were analyzed, the Reynolds and Mach number that corresponds to each section of the blade is shown in Table 4.5. From Figure 4.9, it can be noticed that the increase in the  $C_L$  is more noticeable at higher AoA, while at low AoA, the  $C_L$  variation remains low. At low AoA, the airflow around the blade is more likely to remain smooth without the formation of vortices. Laminar flow is less affected by variations in the Reynolds number compared to turbulent flows.

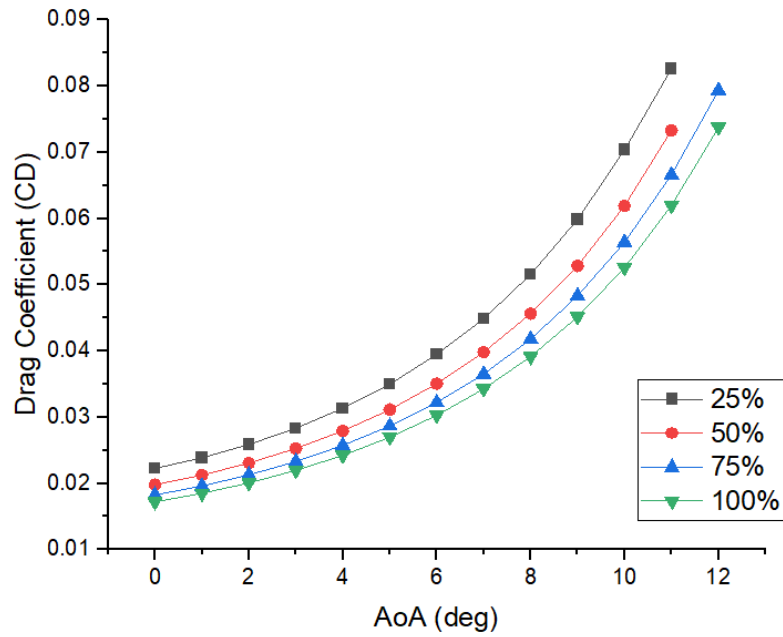


**Figure 4.9.**  $C_L$  variation with the Reynolds number for NACA 8318 clean airfoil.

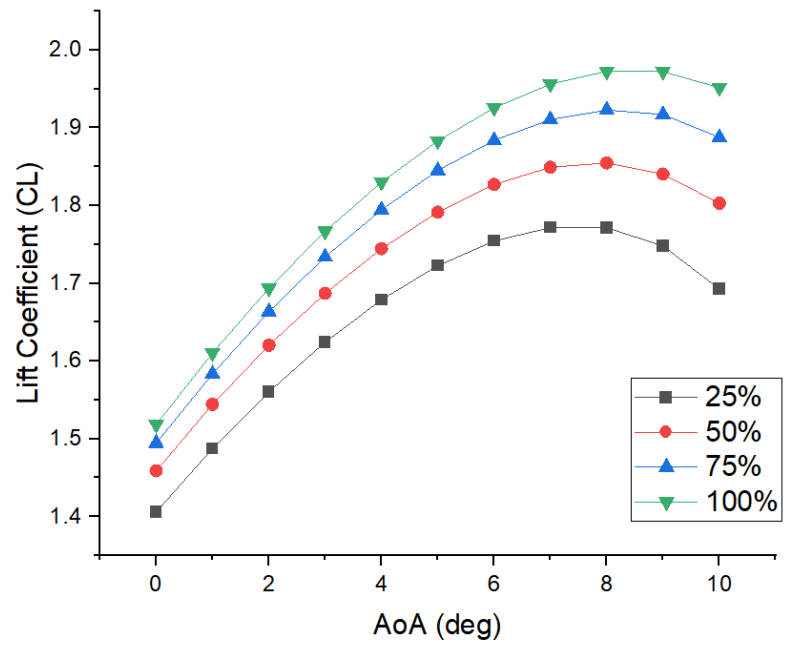
The  $C_L$  and  $C_D$  variations for NACA 8318 with GF at 1% c (Figure 4.10 and 4.11) and GF at 3% c (4.12 and 4.13) show a higher increase trend in the  $C_L$  for airfoil with GF at 5% c even at low AoA while the  $C_D$  tendency seems to remain constant with these two airfoil configurations.



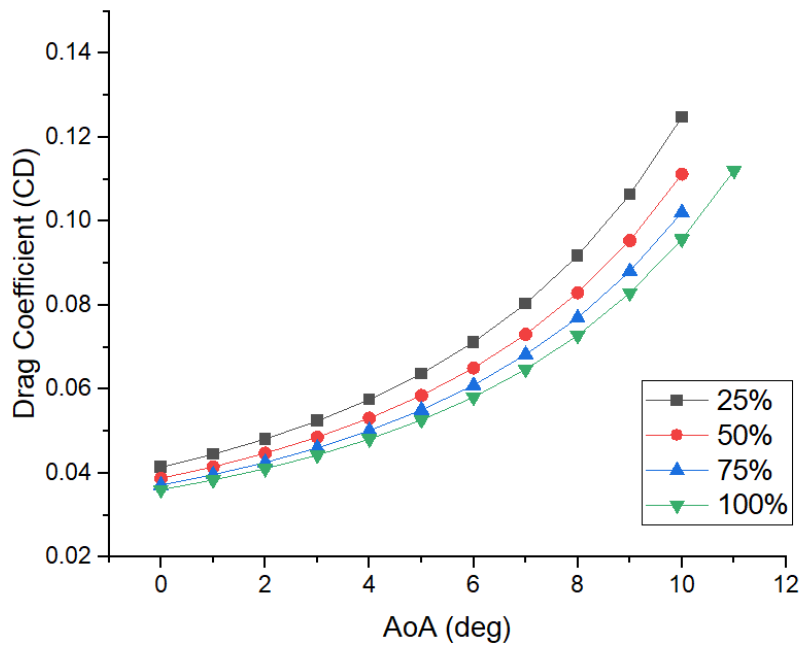
**Figure 4.10.**  $C_L$  variation with the Reynolds number for NACA 8318 with GF at 1%c.



**Figure 4.11.**  $C_D$  variation with the Reynolds number for NACA 8318 with GF at 1%c.

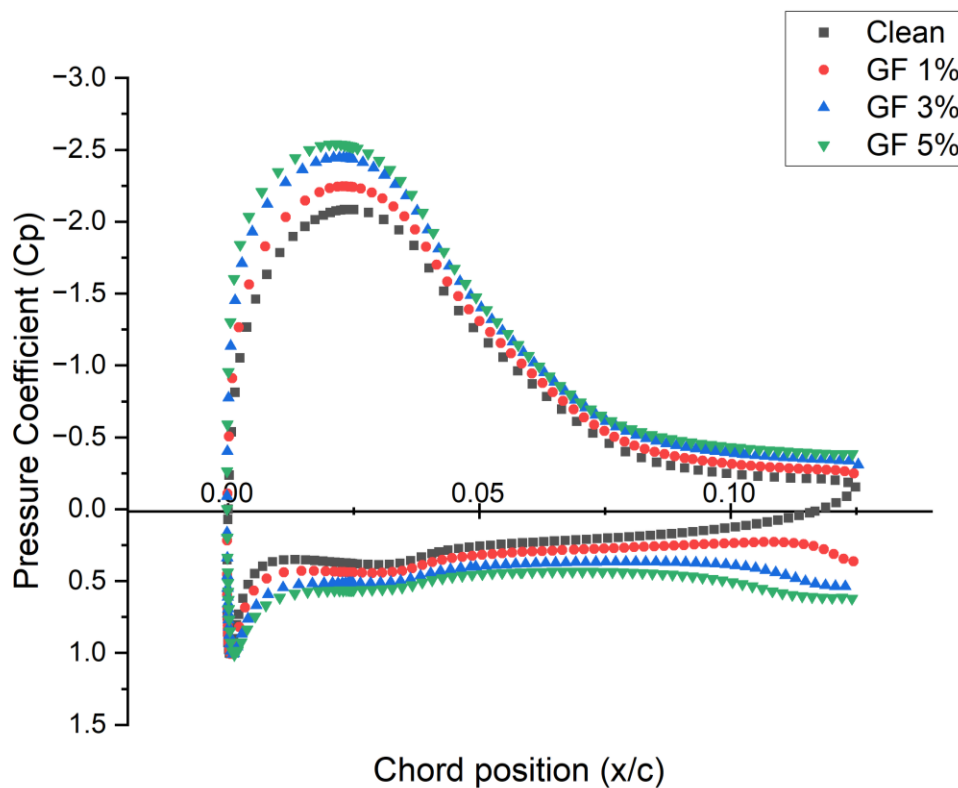


**Figure 4.12.**  $C_L$  variation with the Reynolds number for NACA 8318 with GF at 5%c.



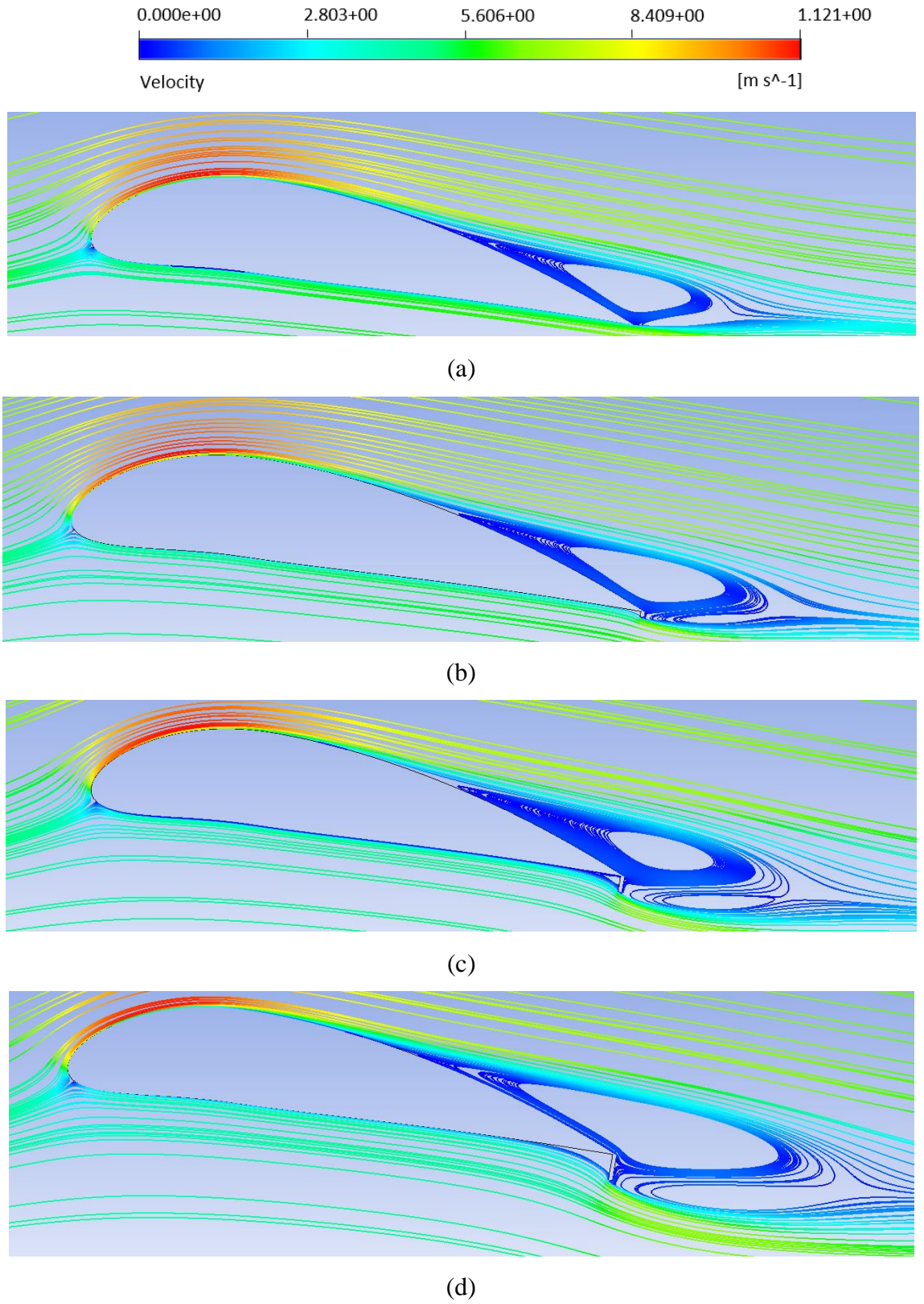
**Figure 4.13.**  $C_D$  variation with the Reynolds number for NACA 8318 with GF at 5%c.

The Pressure Coefficient ( $C_p$ ) along the airfoil illustrated in Figure 4.14, shows an increase in  $C_p$  in the airfoil configurations featuring Gurney flaps (GF). Furthermore, it becomes evident that as the height of the GF increases, the pressure difference, and consequently, the generated lift, also increases. The pressure distribution on airfoils equipped with GF generally follows the trend of the  $C_p$  on a clean airfoil. However, an augmentation in the pressure occurs at the trailing edge where the GF is installed, resulting in a reduction of the adverse pressure gradient.



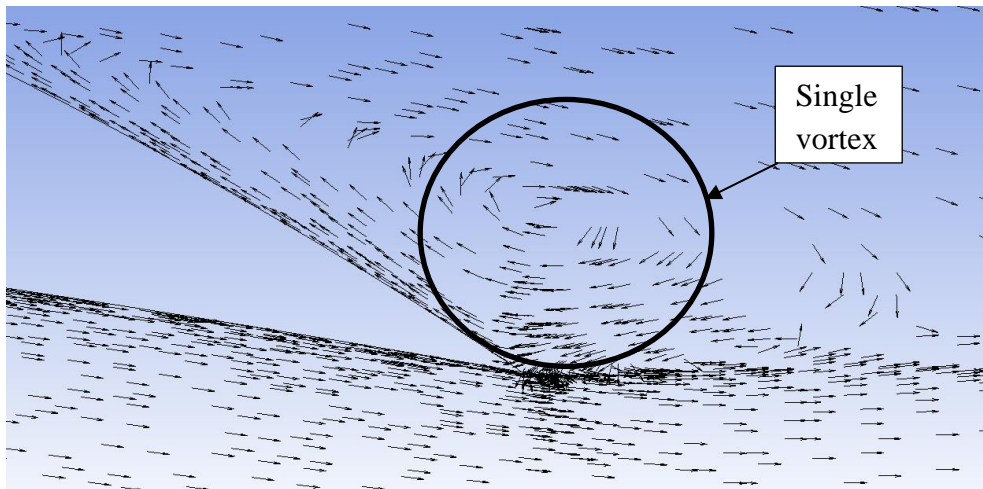
**Figure 4.14.** Pressure coefficient distribution on the airfoil at  $AoA=9$  at  $217,530 Re$  along the chord (m).

Figure 4.15 illustrates the streamlines around the clean airfoil, showing significant flow separation near the trailing edge (T.E.) of the airfoil at  $AoA=9^\circ$ . This separation wake becomes longer as the height of the GF increases. This is a possible explanation for the increase in  $C_D$  with the height of the GF observed in Figure 4.7.

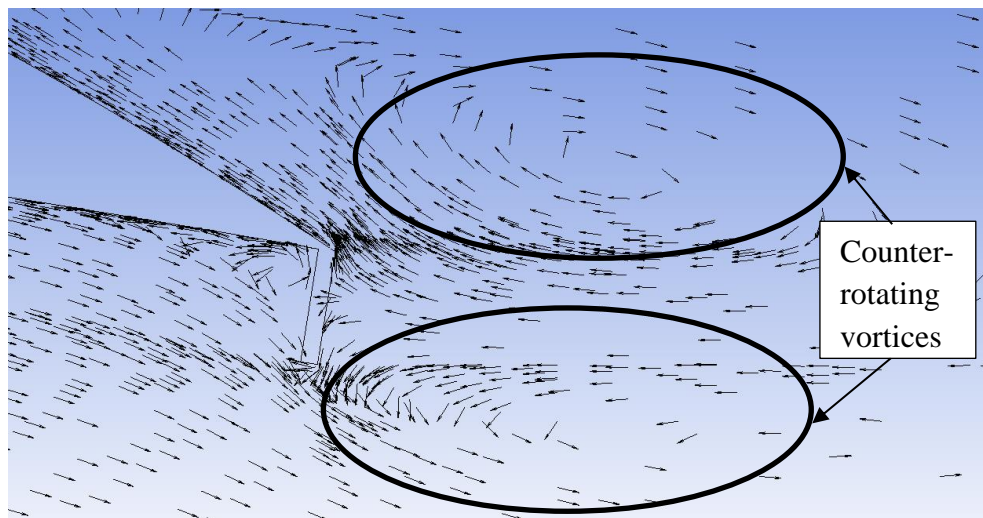


**Figure 4.15.** Flow around the T.E. at AoA=9 degrees for (a) Clean airfoil, (b) GF 1%*c*, (c) GF 3%*c*, (d) GF 5%*c*.

A closer look at the T.E. in Figure 4.16, shows that while for the clean airfoil the separation zone is composed of a single large vortex at the upper surface (Figure 4.16 (a)), the separation zone for 5%*c* GF is composed of two vortices, where the lower one counteracts the upper one (Figure 4.16 (b)). This can explain the lift increase due to the GF addition. In summary, is the upper vortex the one that reduces lift as the separation zone increases and the lower one counteracts the effect.



(a)



(b)

**Figure 4.16.** Vortex formation visualization in the T.E. of (a) Clean airfoil and (b) airfoil with GF at 5%*c* length.

#### 4.2.8 Data validation of NACA 8318

The data for NACA 8318 was validated against experimental data obtained by Yoshida (2000) on a rectangular wing of 0.350 m chord and 2 m span and an aspect ratio of 5.7, the velocity inlet was set up at 20 m/s in X direction, the air properties were set as atmospheric properties.

To determine the ideal mesh cell size, a mesh sensitivity study was conducted, having the first grid point above the wall at  $y^+=0.8, 1, \text{ and } 1.5$ . Table 4.6 displays the outcomes of the mesh sensitivity analysis for NACA 8318 at a Reynolds number of 500k. Discrepancies of 0.04% in  $C_L$  and 0.12% in  $C_D$  were noted among the three mesh configurations. Consequently, it becomes apparent that the distinctions in data across these three meshes are negligible, leading to the selection of the mesh with a  $y^+$  value of 1.

**Table 4.6.** Mesh sensitivity study results for NACA 8318 airfoil at 500k Re at AoA=0 Deg.

$Y^+$	Height of the first grid cell (m)	$C_L$	$C_D$
0.800	$1.24e^{-6}$	$6.779 e^{-1}$	$2.057 e^{-2}$
1	$1.55e^{-6}$	$6.781 e^{-1}$	$2.056 e^{-2}$
1.500	$2.3e^{-5}$	$6.784 e^{-1}$	$2.053 e^{-2}$

Figure 4.17 presents  $C_L$  as function of AoA for the NACA 8318 profile at a Reynolds number of 500k where literature-based experiment data is available. The data contains experimental results obtained by Yoshida (2000), CFD analysis employing the  $k - \omega$  and Transition SST turbulence models, as well as data obtained using BEM software Qblade.

Both turbulence models exhibit good agreement with experimental data,  $k - \omega$  model displays the most accurate  $C_L$  predictions at lower AoA and near the stall angle, whereas the Transition model underestimated  $C_L$  at low AoA but provided more accurate results within the AoA range from 6 to 14. Both models predicted an earlier stall angle in comparison to experimental data. Moreover, despite utilizing fewer computational resources, Qblade software exhibited impressive  $C_L$  prediction capability using Xfoil module (i.e. panel method

with boundary layer correction to account for viscous effects). However, it overestimated  $C_L$  and indicated an earlier stall angle than the experimental data and CFD turbulent models.

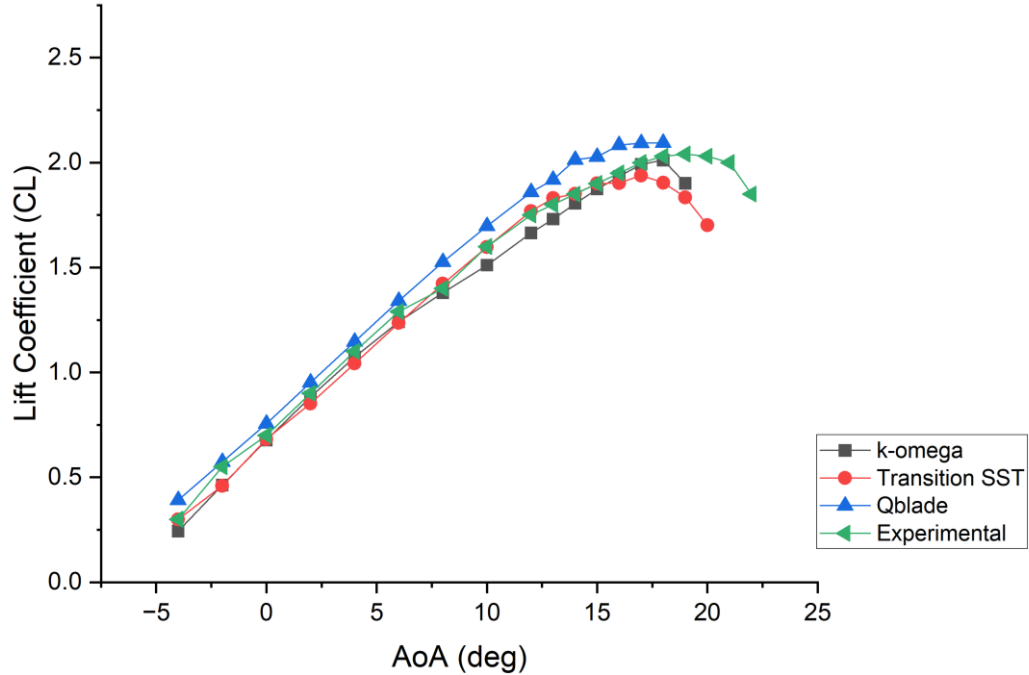


**Figure 4.17.** Comparison of  $C_L$  vs AoA for NACA 8318 at 500k Re at  $M=0.058$ .

### 4.3 E387 Computational

In this section a computational study of the E387 profile was pursued, comparing the CFD results with experimental data made in the low-speed wind tunnel #2 in QMUL. The experimental data was obtained from the work Shen et al. (2016). The work of Aksoy (2020) was considered in the simulation set up, and data was compared for AoA=0 degrees. This section further validates the computational methodology employed for conducting a 2D CFD simulation. Leveraging an earlier validation process, it enables both verification (Aksoy, 2020) and validation (Shen et al., 2016) of the obtained results.

### 4.3.1 Geometry

The airfoil E387 is a low Re airfoil used greatly in HAWT (Shen et al., 2016), the chord the airfoil is of 0.2286 m and the span is 0.76m. For the 2D computational, the airfoil was generated in design modeler in Ansys workbench.

### 4.3.2 Domain

The domain has the same shape and dimensions as the domain used for NACA 8318 CFD. The domain is a C-type shaped inlet, and it is situated 13 chords length away from the trailing edge of the airfoil. The outlet is situated 15 chords away from the trailing edge.

### 4.3.3 Mesh

Table 4.7 illustrates the results of a Mesh sensitivity test using different sizes of Y plus, where we observed slight variations in both  $C_L$  (lift coefficient) and  $C_D$  (drag coefficient). As a result, again, a Y + value of 1 was adopted for subsequent simulations and to calculate the height of the first grid cell. The mesh was generated employing a C-type structured mesh, a Bias function was used to precisely control the initial grid height. In Figures 4.18 and 4.19 the mesh used for this study is illustrated.

**Table 4.7.** Mesh sensitivity study results for E387 airfoil at an angle of attack of 0°.

Y+	Height of the first grid cell (m)	Growth rate	$C_L$	$C_D$
0.8	3.4e-5	1.2	0.3434	0.0164
1	4.2e-5	1.2	0.3419	0.0165
1.5	6.3e-5	1.2	0.3414	0.0165

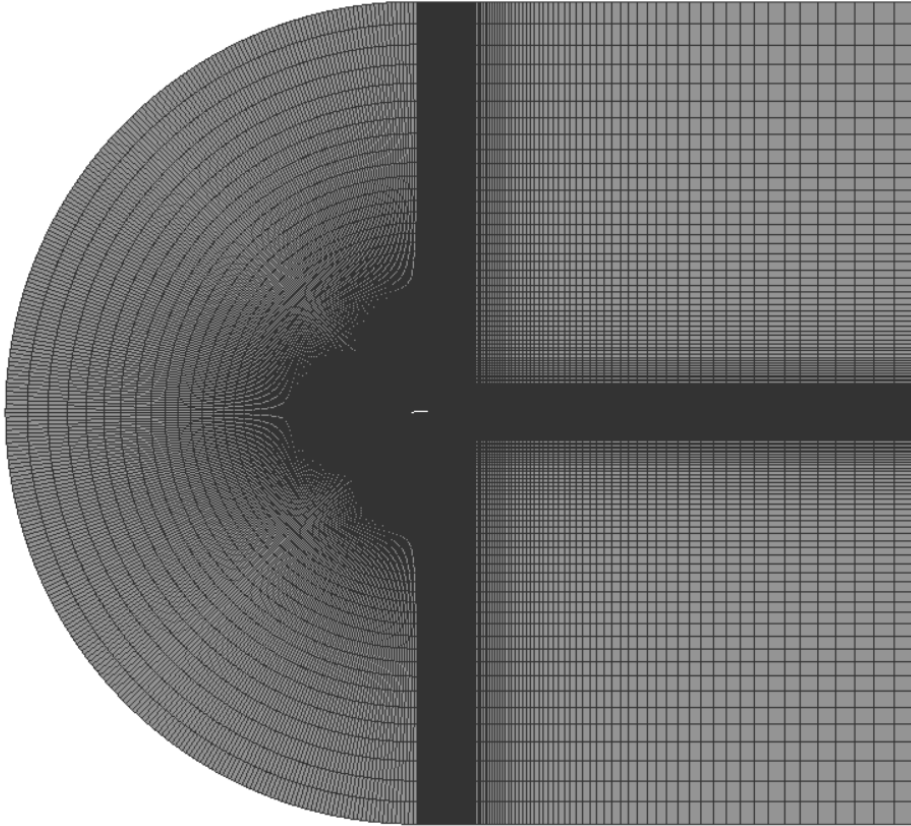


**Figure 4.18.** Overview of structured mesh for E387 airfoil.

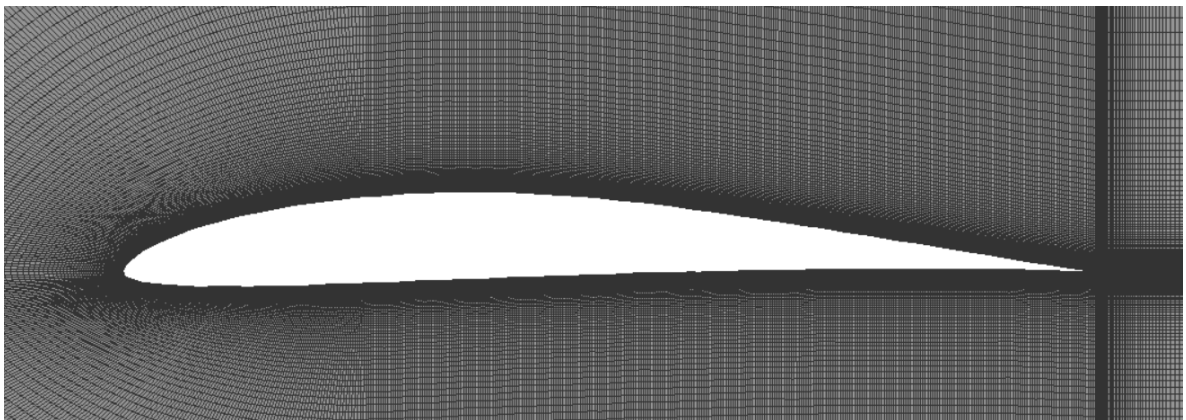


**Figure 4.19.** Detail of structured mesh for E387 airfoil.

### 4.3.4 Boundary conditions

The boundary conditions for E387 simulation were taken from Aksoy (2020) to compare results and verify the CFD simulation process. The inlet velocity was set only in X direction with the value of 6.37 m/s, using a turbulence intensity of 0.61%. The outlet pressure magnitude was set as 101321 Pa.

The airfoil's wall was defined as a stationary surface with a no-slip condition. In the reference values, the area was set as 0.2286 m<sup>2</sup> and the depth was set to 0.76 m. The coupled solution method was employed, and the convergence criteria was adjusted to 10e<sup>-6</sup>.

### 4.3.5 Data validation of E387

The results obtained for the E387 airfoil were compared to experimental data conducted in QMUL low-speed wind tunnel by Shen (2016) and CFD results obtained by Aksoy (2020). Table 4.8 displays the data obtained from the CFD analysis performed for this study and the data obtained from the references. It shows that we have managed to improve the prediction of both C<sub>L</sub> and C<sub>D</sub>.

**Table 4.8.** Data comparison of E873 CFD simulation and experimental test at an angle of attack of 0°.

	Results of performed CFD	CFD results (Aksoy, 2020)	Experimental results (Shen, 2016), as compared to Aksoy (2020)
C <sub>L</sub>	0.3419	0.3707	0.339
C <sub>D</sub>	0.0165	0.0150	0.0202

Figure 4.20 shows the CFD results with the Transition SST and k – ω SST model for E387 at a Re number of 100k, alongside the experimental results obtained by Shen (2016). Both the Transition and k – ω SST models show good agreement, for a low Reynolds number such as 100k, transition SST turbulence model is slightly more accurate than k – ω SST model. Both transitions SST and k – ω models underestimate the C<sub>L</sub> in the AoA range of 8 to 12 degrees and overestimate at low AoA. The C<sub>D</sub> variation with the AoA shown in figure 4.21, shows an overestimation of the C<sub>D</sub> with both turbulence models.

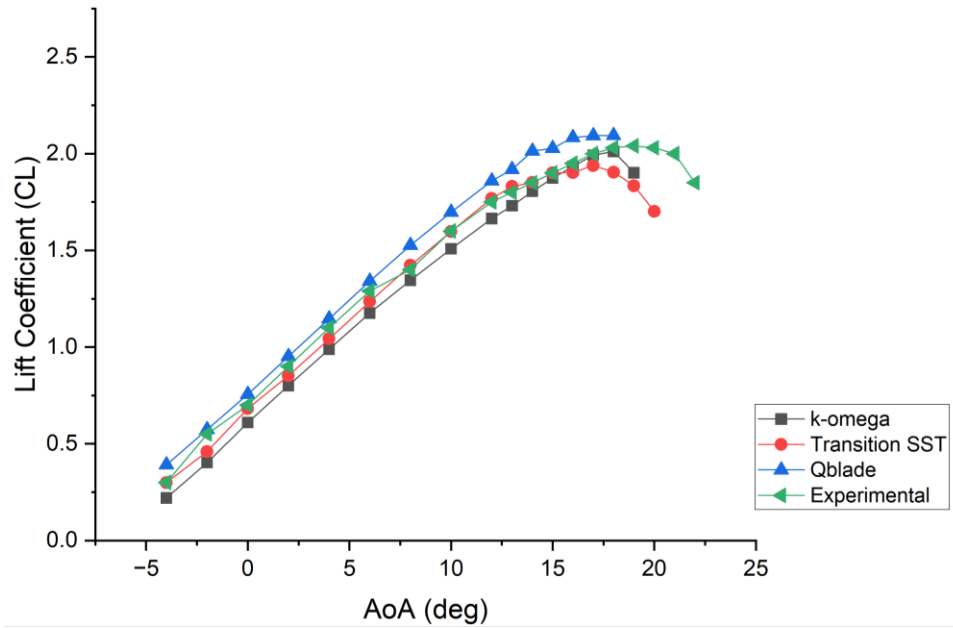


**Figure 4.20.**  $C_L$  vs AoA for E387 at  $Re=100$  k.

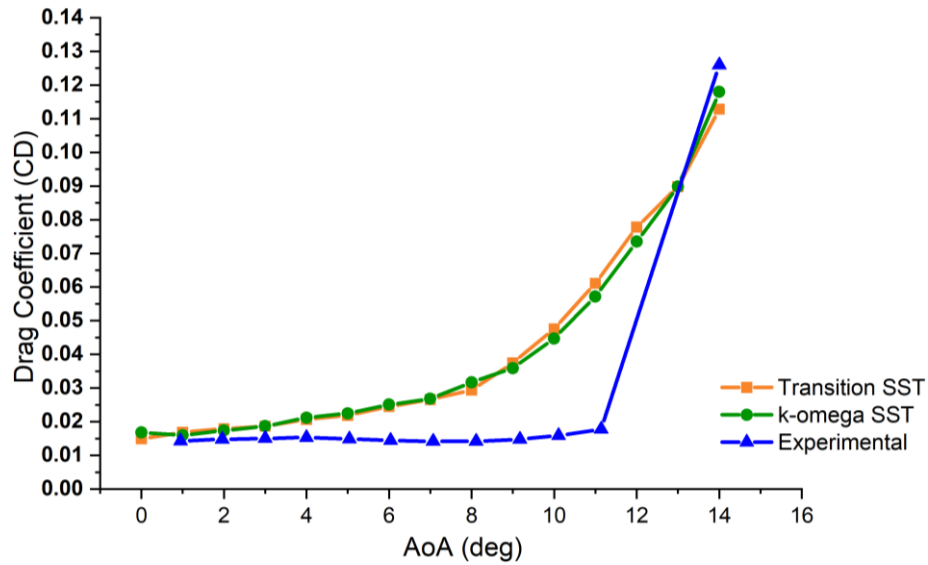


**Figure 4.21.**  $C_D$  vs AoA for E387 at 100k.

Hence, in summary, it was demonstrated that the CFD results for the airfoil aerodynamics in both  $C_L$  and  $C_D$  are acceptable and agree reasonably well with reported results in the literature. Therefore, the CFD results can be used to analyze the turbine performance by leading them into the BEM calculation.

## **4.4 Turbine performance analysis with BEM Method**

Blade Element Momentum codes are commonly utilized to estimate the efficiency on Horizontal Axis Wind Turbines (HAWTs) and Vertical Axis Wind Turbines (VAWTs) across a range of conditions. In comparison to CFD simulations, a BEM simulation is much less time-consuming and much more cost efficient. The BEM method consists in dividing the blade into a finite number of elements and analyzing the aerodynamic force on each element. By summing these forces along the blade span, and considering the rotational effects, the overall efficiency of the turbine can be calculated. However, the Blade Element Momentum (BEM) method relies on simplifications and assumptions, which might affect the accuracy of calculated forces in individual blade elements when compared to a more detailed CFD analysis. To mitigate potential inaccuracies stemming from the BEM method's simplifications, aerodynamic forces on the 2D blade elements were acquired using CFD, enhancing the physical accuracy of the results. Following this, the aerodynamic force data from each blade element was imported into QBlade, aligning with specific sections of the blade (at 25%, 50%, 75%, and 100% locations). This process facilitated the determination of the overall turbine efficiency. By combining the accuracy of CFD results with the time-efficiency of the BEM method, we obtained a more comprehensive estimation of the turbine's overall efficiency.

This section shows the process followed to obtain the turbines efficiency in Qblade. In order to obtain this, a simple model of a turbine needs to be created, so in section 4.4.1 a quick explanation of the method to create the turbine in Qblade is shown. And in section 4.4.2, the results obtained of the hole turbine are shown and analyzed. In section 4.4.2, the power and thrust coefficients are represented as functions of the tip speed ratio (TSR), which can be calculated using equation 3.29. The operational range of TSR for the Ram Air Turbine, determined based on the minimum and maximum conditions outlined in the literature review and summarized in Table 4.11, spans from 2.4 to 3.5.

### **4.4.1 Turbine design in Qblade**

Selecting an airfoil is one of the first steps in BEM simulation. The airfoil NACA 8318 was selected as well as a circular profile for the root of the blades. To create the NACA airfoil, it is necessary to introduce the four or five-digit NACA number as well as the number

of panels in the NACA 4-digit generator option within Qblade. Alternatively, airfoil coordinates can also be imported.

After performing CFD computational RANS in each section of the blade, the  $C_L$  and  $C_D$  variation with AoA were exported to Qblade. Subsequently, this data was extrapolated to larger range of AoA to use these polars at each section of the blade and obtaining the turbine performance. The extension of  $C_L$  and  $C_D$  variations with AoA to the post stall is needed to follow the approximations as in (Ai K. et al., 2016).

Inside the HAWT blade design section in Qblade, a blade can be created using the foils created previously. For the first section, a circular foil was used to create the root of the blade and in the following sections, the airfoil NACA 8318 was used. The specifications of the blade are shown in Table 4.9. In each blade section,  $360^\circ$   $C_L$  and  $C_D$  polars, specific to the Reynolds number of that section, are chosen for further analysis.

**Table 4.9** Blade design specifications.

Position (m)	Chord (m)	Twist (deg)	Foil
0	0.050	60	Circular foil
0.125	0.127	38	NACA 8318
0.250	0.127	20	NACA 8318
0.375	0.127	12	NACA 8318
0.5	0.127	8	NACA 8318

#### 4.4.2 Turbine performance

The BEM analysis section allows to perform an analysis for a range of wind speeds, rotational speeds, and pitch angle. After creating the rotor blades geometry, the simulation was performed at operational conditions shown in table 4.2. The Reynolds numbers used for the BEM simulations at each section of the blade correspond to the Reynolds shown in table 4.5.

Results of the BEM simulation are shown in Figures 4.22, 4.23 and 4.24, where the Power coefficient ( $C_P$ ), Thrust Coefficient ( $C_T$ ) and the Power to Thrust Coefficient ratio variation with the Tip to Speed Ratio (TSR) are illustrated.

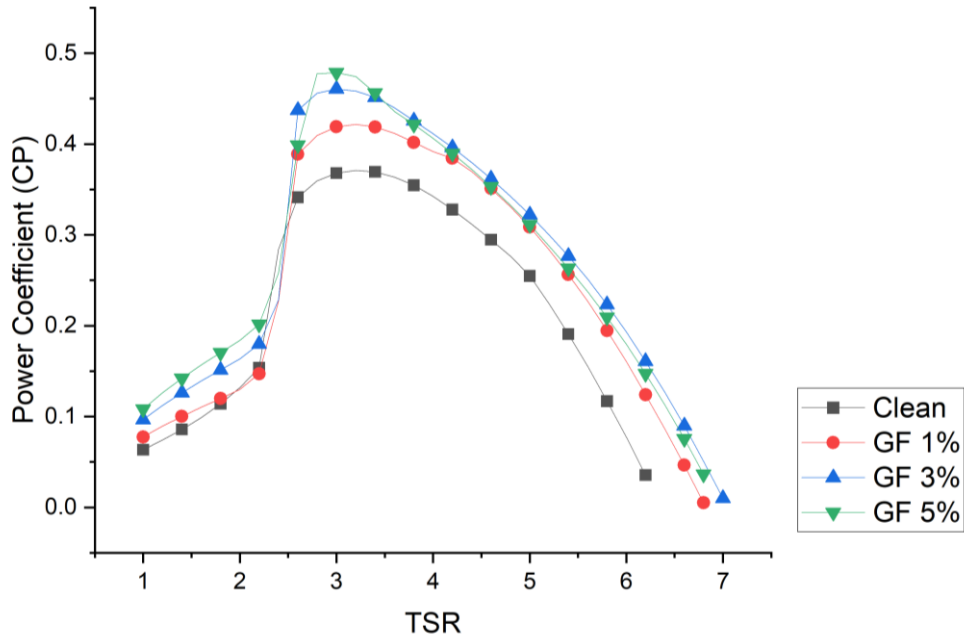
Table 4.10 presents a comparison of Maximum  $C_P$ ,  $C_T$  and  $C_P/C_T$  ratio. The increase of height in the GF resulted in an earlier occurrence of maximum  $C_P$  and a delayed occurrence of maximum  $C_T$ . However,  $C_P/C_T$  ratio remained consistent at the same TSR for clean airfoil blade and blades with GF at 1% and 3% c.

The addition of the GF lead to an increase of the  $C_P$  in the turbine as seen in Figure 4.22. However, as the height of the GF increased, the  $C_T$  also augmented, resulting in a lower Maximum  $C_P/C_T$  ratio for the turbines equipped with GF.

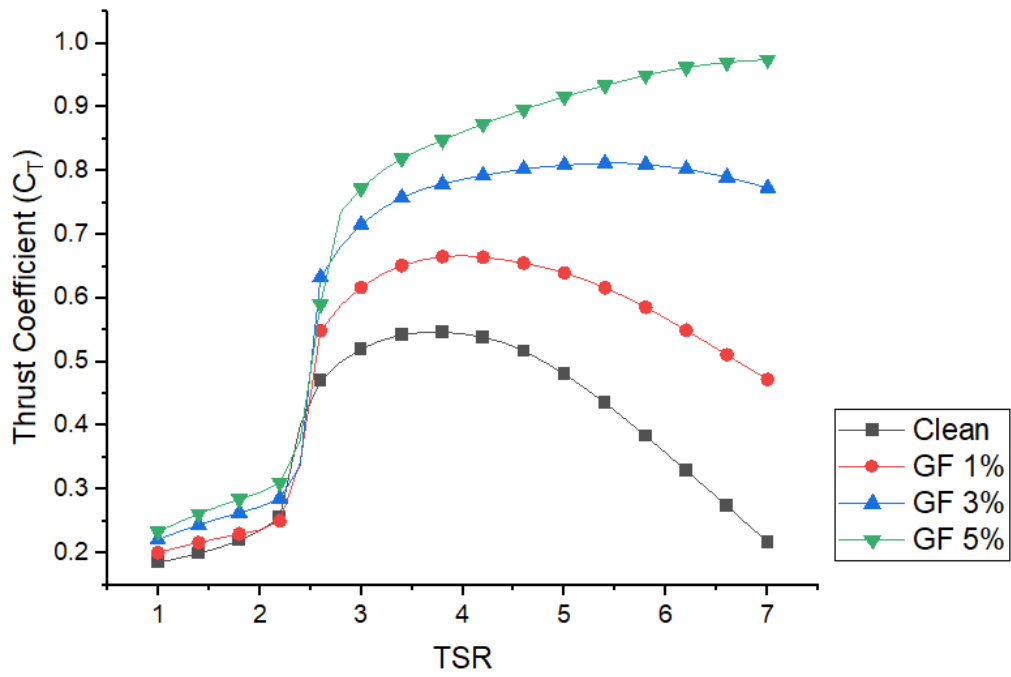
Nevertheless, Figure 4.24 highlights a significant increase of 22% and 26% in the  $C_P/C_T$  ratio within the TSR range of 1 to 2.5 for GF heights of 3% and 5% c, respectively, while the smaller GF of 1% have a maximum increase of 11% and 314% for TSR values ranging from 1 to 1.8 and 5.8 to 6.8 respectively. However, the TSR range displaying an increase falls outside the operational range of the Ram Air Turbine (RAT) under study.

**Table 4.10.** Comparison of maximum  $C_P$ ,  $C_T$  and  $C_P/C_T$  ratio for four blade configurations at different TSR.

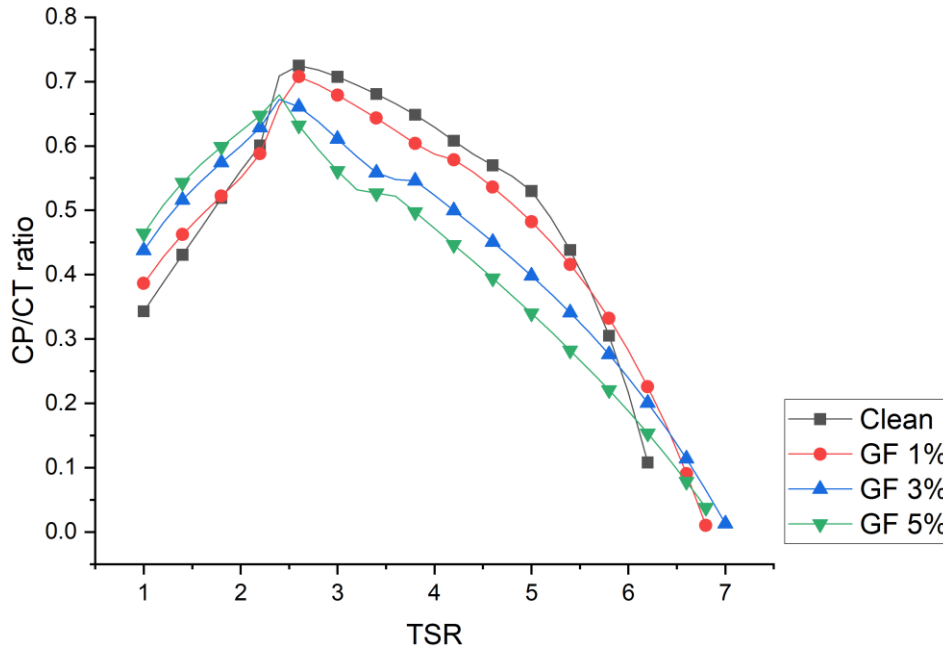
Blade configuration	TSR	Max $C_P$	TSR	Max $C_T$	TSR	Max $C_P/C_T$ ratio
Clean airfoil	3.2	0.371	3.8	0.547	2.6	0.725
GF 1% c	3.2	0.422	4	0.667	26	0.708
GF 3% c	3	0.461	5.4	0.812	2.6	0.691
GF 5% c	3	0.478	7.4	0.976	2.4	0.685



**Figure 4.22.** Power Coefficient variation with TSR for airfoil without and with GF at heights of 1%, 3% and 5% c.



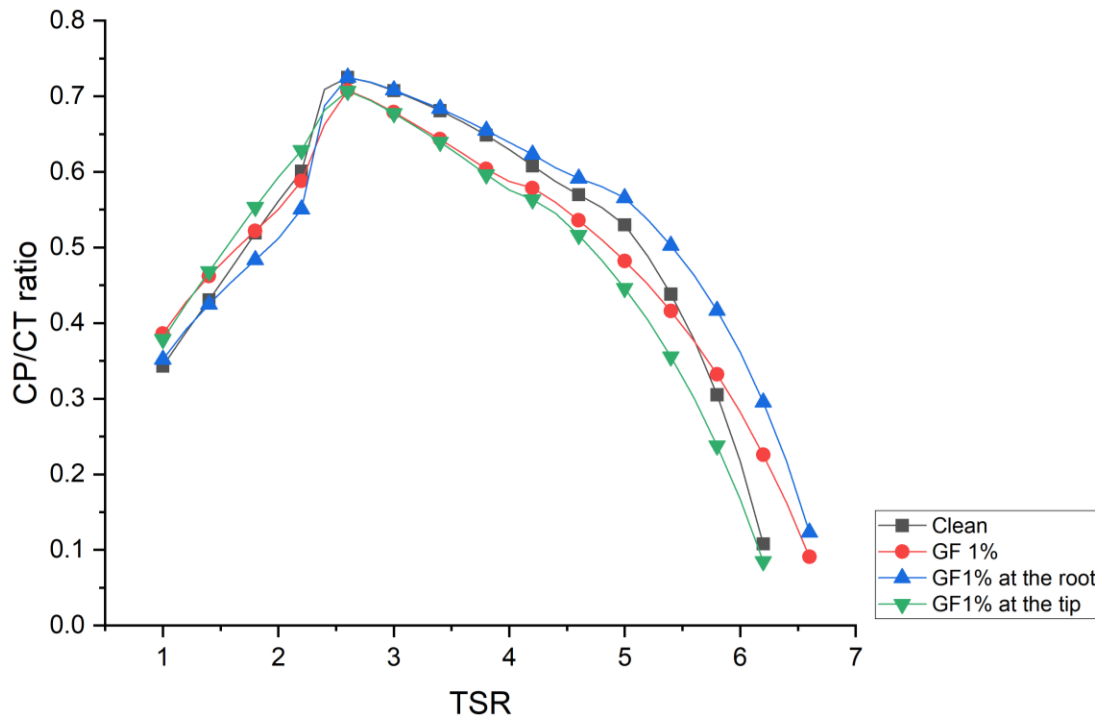
**Figure 4.23.** Thrust Coefficient variation with TSR for Turbine blades without and with GF at heights of 1%, 3% and 5% c.



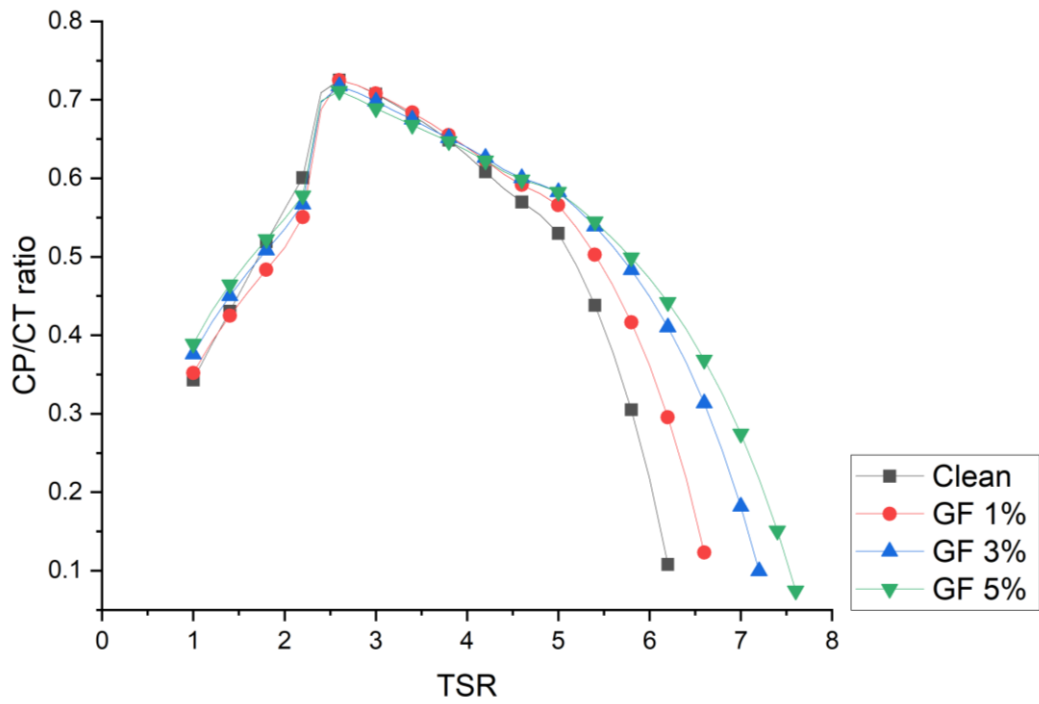
**Figure 4.24.** Pressure Coefficient to Thrust Coefficient ratio vs TSR for turbine blades without and with GF at heights of 1%, 3% and 5%*c*.

Figure 4.24 reveals that the  $C_P/C_T$  ratio experiences significant improvement at a narrow range of TSR (1 to 1.5 approx.) for blades with GF. Nevertheless, the Ram Air Turbine (RAT) under investigation operates within a TSR range of 2.4 to 3.5. Therefore, the depicted increase in the TSR range illustrated in Figure 4.24 is not pertinent to the operational conditions considered in this study. Furthermore, the application of the Gurney flap (GF) can be limited to specific sections of the blade to enhance the efficiency in a wider range of TSR. In Figure 4.25, a blade configuration is presented, showcasing the GF mounted exclusively at either the root (25 to 50%) or the tip (50 to 100%) of the blade, in contrast to a constant GF along the entire blade and a completely clean blade.

When the GF is mounted solely at the blade's root, it enhances the  $C_P/C_T$  ratio over a broader TSR range, spanning from 2.6 to 6.6, with the maximum  $C_P/C_T$  ratio occurring at 2.6 TSR. On the other hand, when the GF is applied only at the tip of the blade, it enhances turbine performance within a lower tip speed ratio range, specifically from 1 to 2.4, as demonstrated in Figure 4.25.



**Figure 4.25.**  $C_P/C_T$  ratio comparison for GF height of 1%c mounted at either the root or the tip of the blade and original blade.



**Figure 4.26.**  $C_P/C_T$  ratio comparison for original blade and different blade configurations with GF with heights of 1%, 3% and 5%c mounted at the root of the blade.

Since the most effective blade configuration with the Gurney flap was found to be at the root of the blade, a comparison was made between a clean blade and blade with GF mounted only at the root, as illustrated in Figure 4.26. Notably, a GF representing 1% of the chord yields improved  $C_P/C_T$  for a wider range of TSR from 2.6 to 6.6. However, a GF with height of 5%c exhibits the highest  $C_P/C_T$  ratio, both at low TSR (ranging from 1 to 2.4) and high TSR (from 4 to 6.2). In accordance with the operational conditions outlined in Table 4.11, the optimal blade configuration for the Ram Air Turbine (RAT) involves a blade with a Gurney Flap (GF) positioned at 1% chord length, exclusively mounted at the root of the blade.

## 4.5 Summary

In this chapter an insight into the aerodynamics of the airfoil NACA 8318 was shown to study the effect of the addition of a Gurney Flap in the airfoil by performing two-dimensional CFD. It was shown that the lift coefficient as well as the drag coefficient of the airfoil increase as the height of the Gurney flap does. For GF heights of 3% and 5%c the lift to drag ratio (Figure 4.8) is higher than the clean airfoil from a range of  $0 < \text{AoA} < 5$  degrees and  $0 < \text{AoA} < 3$  degrees respectively. For the GF height of 1%c, the  $C_L/C_D$  ratio showed an increment for a wider range from an AoA of 0 to 9 degrees. At low AoA the GF 1%c, showed similar drag coefficients to the original profile.

The turbine analysis using BEM method, presented in section 4.4, demonstrated improved  $C_P/C_T$  performance at low TSR values for RAT with GF along the entire length of the blade, ranging from 1 to 2.2 for turbine with GF of 3%c and from 1 to 2.4 TSR for turbine with GF of 5%c, however, at TSR value of 2.6, where the maximum  $C_P/C_T$  is achieved, the original bladed turbine has shown a better performance (Figure 4.22). As the operational TSR range for the studied turbine spans from 2.4 to 3.5, it becomes evident that the turbine's performance, equipped with a Gurney Flap along the entire blade, does not align adequately with these specified operational conditions.

Furthermore, the turbine with GFs mounted only at the blade's root showed better performance in the TSR operational range with a higher  $C_P$  to  $C_T$  ratio in a wider range of TSR ranging from 1 to 1.8 and 4 to 7.6 for blade with GF 5%c, and 2.6 to 6.6 for GF 1%c as shown in Figure 4.26. The maximum  $C_P$  occurred at the same TSR of 2.6 for all the blades

configurations, but only blades with GF 1%*c* showed a slight enhance of 0.018% in the mentioned TSR, after that point, the  $C_P/C_T$  ratio for all GF configurations resulted in an increase, demonstrating that the turbine with GF mounted solely at the blade's root, increase the  $C_P$  to  $C_T$  ratio at high TSR.

Taking into consideration the maximum and minimum operational conditions of commercial RATs as listed in Table 4.11, the operational TSR range falls between 2.4 to 3.5. Considering this, the turbine configuration with a GF of 1%*c* located at the blade's root proves to be the preferred choice, as it exhibits an improved  $C_P/C_T$  ratio within the TSR range of 2.6 to 6.6 as shown in figure 4.26 and shows a maximum  $C_P/C_T$  of 0.018% higher than the original turbine.

**Table 4.11.** Minimum (Saad et al., 2017) and maximum operating condition for RAT.

	Minimum condition	Maximum condition
Flight height	6000 m	10,000 m
Angular speed	2800 RPM	3800 RPM
Flight speed	41.16 m/s	82.31 m/s

## Chapter 5

### 5. Conclusions and Future work

#### 5.1. Discussion and conclusions

The following section presents the discussion of the results of the computational analysis conducted in this study. It is important to note that the results obtained in this study are specific to the analysis performed and may vary from other studies or experimental data. The purpose of this analysis was to investigate and understand the behavior of the system under the given conditions for this study. Therefore, any discrepancies or differences observed should be interpreted within the context of this particular analysis. It is essential to consider these results as a contribution to the overall understanding of the behavior of NACA 8318 airfoil under the conditions presented in this study rather than an absolute representation of its behavior. Extensive CFD simulations were conducted using the same process as the validation process described in Section 4.2.8.

The research presented in this study explores the effect of adding a Gurney Flap (GF) at different heights of 1%, 3% and 5% of the chord length at the Trainling Edge (T.E.) of NACA 8318 profile, by performing two-dimensional Reynolds Average Navier Stokes (RANS) analysis in the software Ansys fluent, using the turbulence model  $k - \omega$  Shear Stress Transport (SST). The results presented in chapter 4, provide evidence of the Lift coefficient ( $C_L$ ) increment with the increase of the Gurney Flaps height, however, this also led to an increase in the Drag coefficient ( $C_D$ ). After the two-dimensional analysis, the aerodynamic coefficients were exported to Qblade software to obtain the overall efficiency of the turbine with the Blade Element Momentum method.

The Gurney Flap at height of 1% of the chord of the airfoil, showed a higher Lift to Drag coefficient ratio in comparison to the other GF heights (3%c and 5%c). This means, that a GF of 1% chord (1%c) effectively enhances lift without significantly raising drag to a level that offsets the advantage gained from the increased lift. At a Reynolds number of 217,530, the NACA 8318 clean airfoil and with GF (at 1%, 3% and 5%c) showed an

increment of the Lift to Drag ratio at ranges of  $0 < \text{AoA} < 9$  for GF 1%c,  $0 < \text{AoA} < 5$  for GF 3%c and  $0 < \text{AoA} < 3$  for GF 5%c, being AoA the angle of attack of the airfoil.

In addition to that, the Blade Element Momentum (BEM) analysis showed an increase in the power to thrust coefficient ( $C_P / C_T$ ) ratio was observed within the tip speed ratio (TSR) range of 1 to 2.2 for GF heights of 3% and from 1 to 2.4 5%c, while the smaller GF of 1% showed an increase of 11% and 314% within the ratio for TSR values ranging from 1 to 1.8 and 5.8 to 6.8, respectively, for turbines with GF mounted along the whole blade. These findings indicate that incorporating a Gurney flap along the blade doesn't offer benefits within the specific operational conditions considered, spanning a TSR (Tip Speed Ratio) range from 2.4 to 3.5.

After analyzing the effect of the GF mounted along the blade, a BEM analysis of the GF mounted only at the root of the blade was made, showing a higher  $C_P / C_T$  ratio for GF at 1%c at a wider range of TSR (from 2.6 to 6.6), however, a GF with height of 5%c exhibits the highest  $C_P / C_T$  ratio with a maximum increment of 11.832% and 75.577%, both at low TSR (ranging from 1 to 1.8) and high TSR (from 4 to 7.6) respectively.

Considering these findings, the most effective Gurney flap configuration for the Ram Air Turbine operating within a tip speed ratio range of 2.4 to 3.5 is the one set at 1% chord (1%c). This configuration demonstrates a 0.018% increase in the Maximum Power to Thrust coefficient ratio. Notably, it exhibits an enhancement of 0.639% at a Tip Speed Ratio (TSR) of 3.5, and remarkably achieves a maximum enhancement of 257.598% at a TSR of 6.6. It's important to note that the increment at TSR 6.6 falls beyond the operational TSR conditions studied. However, this highlights the Gurney Flap's superior performance at higher TSR values. Higher TSR values correspond to lower air speeds, indicating that implementing a Gurney Flap proves more beneficial in turbines operating at very low speeds.

## **5.2. Future work recommendations**

In the pursuit of enhancing the performance and efficiency of Ram Air Turbines (RATs), this study has explored the effects of the GF addition into the turbine design. The utilization of GF, strategically positioned at the root of the turbine's blade, has demonstrated

its potential to improve aerodynamic efficiency. However, there is a variety of future work recommendations that can be implemented in the future.

As shown in this study, the increase of the Drag coefficient ( $C_D$ ) as well as the Lift coefficient ( $C_L$ ) was more noticeable in Gurney Flaps (GF) of 5% $c$  height. The introduction of slits in the GF along the blade emerges as a promising strategy. It is important to recognize that a comprehensive analysis of slitted GF effects cannot be adequately addressed through 2D computational studies alone. Consequently, the recommendation stands for the pursuit of 3D computational studies to thoroughly investigate the impact of a slitted GF along the blade.

While RANS simulations have been shown to yield accurate results in comparison to experimental data, it is worth noting that the RANS model may exhibit inaccuracies, particularly in predicting the  $C_D$ . Therefore, conducting experimental tests on blades equipped with GF would be highly advantageous and is recommended for a more comprehensive validation of aerodynamic performance.

Finally, as highlighted in the earlier section 5.1, the Gurney Flap exhibits superior performance at lower speeds. Consequently, this suggests that a turbine operating under low-speed conditions, such as a terrestrial wind turbine, will benefit more from the incorporation of a Gurney Flap compared to a Ram Air Turbine operating at higher speeds.

## 6. List of references

- Abir, A., Mehdi, D., & Lassaad, S. (2017). Pitch angle control of the variable speed wind turbine. *2016 17th International Conference on Sciences and Techniques of Automatic Control and Computer Engineering, STA 2016 - Proceedings, 1(2)*, 582–587. <https://doi.org/10.1109/STA.2016.7952021>
- Ai K., Avital E. J., Korakianitis T., Samad A., & Venkatesan N. (2016). *Surface Wave Effect on Marine Current Turbine, Modelling and Analysis*.
- Akagi, R. M. (2021). *Ram Air Turbine of minimum drag. 3(2)*, 1–10.
- Aksoy, O. M. (2020). *CFD Analysis of the Aerodynamic Effects of a Gurney Flap on a Small-Scale Horizontal Axis Wind Turbine with a Low Reynolds Number*.
- Altoma, A. S., & Alhakeem, M. R. H. (2019). Design and Simulation of Electrical Emergency System in Aircraft using Ram Air Turbine. *2018 IEEE International Conference on Electrical Systems for Aircraft, Railway, Ship Propulsion and Road Vehicles and International Transportation Electrification Conference, ESARS-ITEC 2018*, 1–6. <https://doi.org/10.1109/ESARS-ITEC.2018.8607299>
- Andersson, B., Andersson, R., Håkansson, L., Mortensen, M., Sudiyo, R., & Van Wachem, B. (2011). Computational fluid dynamics for engineers. In *Computational Fluid Dynamics for Engineers*. <https://doi.org/10.1017/CBO9781139093590>
- Bolognesi, P., Papini, F., & Taponecco, L. (2009). *Hybrid-Excitation DC Machines as Highly Reliable Generators for Ram Air Turbines*.
- Cengel, Y. A. (2006). *Fluid Mechanics*.
- Cosner, R. R., Louis, S., & Analysis, C. F. D. (1994). *Issues in Aerospace Application of CFD Analysis Mzonnell Douglas Aerospace 32nd Aerospace Sciences Meeting & Exhibit*.
- Dewan, A. (1967). Tackling Turbulent Flows in Engineering. In *Angewandte Chemie International Edition, 6(11)*, 951–952. (Vol. 13).
- ElQatary, I., & Elhadidi, B. (2013). Comparison of CFD with BEM technique for wind turbine simulation of thin and thick rotor blades. *31st AIAA Applied Aerodynamics Conference*, 1–10. <https://doi.org/10.2514/6.2013-2417>
- Gundtoft, S. (2009). *Wind turbines*.
- Harrington, E., & Baines, A. N. (2019). *Ram Air Turbine Blades* (Patent US 2019/0017492).

- Jang, C. S., Ross, J. C., & Cummings, R. M. (1998). Numerical investigation of an airfoil with a Gurney flap. In *Aircraft Design* (Vol. 1).
- Jian, W. (2016). Research on several similarity criteria of ram air turbine operating under high-low altitude. *AUS 2016 - 2016 IEEE/CSAA International Conference on Aircraft Utility Systems*, 141–145. <https://doi.org/10.1109/AUS.2016.7748036>
- Jiménez-Ramírez, A., López-Garza, V., & Molinero-Hernández, Daniel Casillas-Farfán, C. (2016). Metodología de Diseño del Perfil Aerodinámico de Hub para Turbinas de Viento de Eje Horizontal de Baja Capacidad. *Revista de Aplicaciones de La Ingeniería*, 3(9), 9–25.
- J.J. Wang, Y.C. Li, & K.-S. Choi. (2007). Gurney flap—Lift enhancement, mechanisms and applications. *Elsevier*, doi:10.1016/j.paerosci.2007.10.001.
- John D. Anderson, Jr. (2012). Fundamentals of Aerodynamics (in SI units). In *The Aeronautical Journal* (Vol. 116, Issue 1176).
- Li, Y., Wang, J., & Zhang, P. (2002). Effects of Gurney Flaps on a NACA0012 Airfoil. In *Flow, Turbulence and Combustion* (Vol. 68).
- M. F. Ismail. (2014). Aerofoil profile modification effects for improved performance of a vertical axis wind turbine blade. *School of Mechatronic Systems Engineering, Simon Fraser University*, 1–80.
- Manwell, J. F. (2002). *Wind energy explained*.
- Manyonge, A. W., Manyala, R., Shichika, J., Manyonge, A. W., Ochieng, R. M., Onyango, F. N., & Shichikha, J. M. (2012). Mathematical Modelling of Wind Turbine in a Wind Energy Conversion System: Power Coefficient Analysis Well water pumping using wind energy energy system for enhanced food security and health View project Mathematical Modelling of Wind Turbine in a Wind En. *Applied Mathematical Sciences*, 6(91), 4527–4536. <https://www.researchgate.net/publication/235525719>
- Marten, D., & Wendler, J. (2013). *QBlade Guidelines - v0.6*. 76. [https://sourceforge.net/projects/qblade/files/Guidelines/QBlade\\_Guidelines\\_v05.pdf/download](https://sourceforge.net/projects/qblade/files/Guidelines/QBlade_Guidelines_v05.pdf/download)
- Maughmer, M. D., & Bramesfeld, G. (2008). Experimental investigation of Gurney flaps. *Journal of Aircraft*, 45(6), 2062–2067. <https://doi.org/10.2514/1.37050>
- Parés Prat, A. (2012). *Use of Ram Air Turbines for electrical taxiing in Airbus 320*
- Renganathan, S. A., Denney, R., Duquerrois, A., & Mavris, D. (2014). Validation and assesment of lower order aerodynamics based design of Ram Air Turbines. *12th*

- International Energy Conversion Engineering Conference, IECEC 2014*, 1–16. <https://doi.org/10.2514/6.2014-3463>
- Ryu, J., Kim, S. S., & Kim, S. S. (1994). A General Approach to Stress Stiffening Effects on Flexible Multibody Dynamic Systems. *Mechanics of Structures and Machines*, 22(2), 157–180. <https://doi.org/10.1080/08905459408905209>
- Saad, M. M., Mohd, S. Bin, & Zulkafli, M. F. (2017). A survey on the use of ram air turbine in aircraft. *AIP Conference Proceedings*, 1831. <https://doi.org/10.1063/1.4981189>
- Schubel, P. J., & Crossley, R. J. (2012). Wind turbine blade design. *Energies*, 5(9), 3425–3449. <https://doi.org/10.3390/en5093425>
- Sharma, P., Gupta, B., Pandey, M., Sharma, A. K., & Nareliya Mishra, R. (2021). Recent advancements in optimization methods for wind turbine airfoil design: A review. *Materials Today: Proceedings*, 47, 6556–6563. <https://doi.org/10.1016/j.matpr.2021.02.231>
- Shen, X., Korakianitis, T. K. A., Theodosios, A., & Avital, E. (2016). *Experimental and Numerical Study of Surface Curvature Effects on the Performance of the Aerofoils Used in Small Wind Turbines*.
- Singh, R. K., & Ahmed, M. R. (2013). Blade design and performance testing of a small wind turbine rotor for low wind speed applications. *Renewable Energy*, 50, 812–819. <https://doi.org/10.1016/j.renene.2012.08.021>
- Sustainable Aviation (SA). (2020). *NET ZERO CARBON ROAD-MAP SUMMARY REPORT*.
- Syawitri, T. P., Yao, Y., Yao, J., & Chandra, B. (2022). Geometry optimisation of vertical axis wind turbine with Gurney flap for performance enhancement at low, medium and high ranges of tip speed ratios. *Sustainable Energy Technologies and Assessments*, 49. <https://doi.org/10.1016/j.seta.2021.101779>
- Tachos, N. S., Filios, A. E., Margaris, D. P., & Kaldellis, J. K. (2009). A computational aerodynamics simulation of the NREL phase II rotor. *Open Mechanical Engineering Journal*, 3, 9–16. <https://doi.org/10.2174/1874155X00903010009>
- Transportation Safety Board of Canada. (2017). *Avionics compartment fire, Air Canada, Embraer ERJ 190-100 IGW, C-FHOS, Boston, Massachusetts, United States, 97 nm WNW, 25 May 2016*. Transportation Safety Board of Canada.
- Valencia, E., Berrazueta, M., Leines, D., Lema, H., Rodriguez, D., & Hidalgo, V. (2020). Aerodynamic design and testing of a ram air turbine for small fixed-wing uavs. *AIAA Propulsion and Energy 2020 Forum*, 1–15. <https://doi.org/10.2514/6.2020-3957>

- Walter, M., & Mavris, D. N. (2016). Sequential robust design of a ram air turbine. *17th AIAA/ISSMO Multidisciplinary Analysis and Optimization Conference*. <https://doi.org/10.2514/6.2016-4408>
- Wang, J., Lu, Y. L., & Zhai, X. T. (2015). Research on Ram Air Turbine Blade Properties. *Applied Mechanics and Materials*, 779, 117–124. <https://doi.org/10.4028/www.scientific.net/amm.779.117>
- Wang, L., Quant, R., & Kolios, A. (2016). Fluid structure interaction modelling of horizontal-axis wind turbine blades based on CFD and FEA. *Journal of Wind Engineering and Industrial Aerodynamics*, 158, 11–25. <https://doi.org/10.1016/j.jweia.2016.09.006>
- White, F. M. (2011). Fluid Mechanics. In M. G. Hill (Ed.), *Power* (Seventh ed).
- Xia, T., Zhang, D., & Lu, Y. (2018). Study on the rotation speed control method for Ram Air Turbine System. *IET Conference Publications*, 2018(CP743), 460–465. <https://doi.org/10.1049/cp.2018.0298>
- Yan, Y. (2020). *Aerodynamic performance improvement of vertical axis wind turbines through novel techniques*.
- Yang, S., & Liang, Z. (2010). Numerical simulation of the unsteady flow and power of horizontal axis wind turbine using sliding mesh. *Asia-Pacific Power and Energy Engineering Conference, APPEEC*, 7–9. <https://doi.org/10.1109/APPEEC.2010.5448767>
- Yoshida. (2000). *Adverse reynolds number effect on maximum lift of two dimensional airfoils. Advanced Technology Aircraft Project Center NATIONAL AEROSPACE LABORATORY6-13-1 Osawa, Mitaka, Tokyo 181-0015 JAPAN*Keywords: transition, short bubble, turbulent separation, NACA 8318, wind tunnel test.
- Zhang, X., Ding, S., Du, F., Ji, F., & Guo, S. (2018). *Numerical Simulation on Aerodynamic Performance of Ram Air Turbine Based on Mixed Flow Field*. 1–8. <https://doi.org/10.1115/imece2018-88304>
- Zhang, Y., Ramdoss, V., Saleem, Z., Wang, X., Schepers, G., & Ferreira, C. (2019). Effects of root Gurney flaps on the aerodynamic performance of a horizontal axis wind turbine. *Energy*, 187. <https://doi.org/10.1016/j.energy.2019.115955>